Supporting information for: Photon Reabsorption Masks Intrinsic Bimolecular Charge-Carrier Recombination in $CH_3NH_3PbI_3$ Perovskite

Timothy W. Crothers,[†] Rebecca L. Milot,[†] Jay B. Patel,[†] Elizabeth S. Parrott,[†] Johannes Schlipf,[‡] Peter Müller-Buschbaum,[‡] Michael B. Johnston,[†] and Laura M. Herz[*,†]

†*Department of Physics, University of Oxford, Clarendon Laboratory, Parks Road, Oxford OX1 3PU, United Kingdom*

‡*Lehrstuhl für Funktionelle Materialien, Physik-Department, Technische Universität München, James-Franck-Str. 1, 85748 Garching, Germany*

E-mail: laura.herz@physics.ox.ac.uk

Contents

1 Material Preparation

1.1 Cleaning of Substrates

z-cut quartz substrates were cleaned with hellmanex solution, followed by a rinse with distilled water. The substrate was then twice washed with acetone, isopropanol, and ethanol. Thereafter the substrates were plasma etched in O_2 for 10 minutes.

1.2 Thermal Co-Evaporation of $CH_3NH_3PbI_3$ ($MAPbI_3$).

Thin films of $MAPbI_3$ were fabricated using thermal evaporation as reported previously.[S1] In brief, the tooling factor was determined by depositing the starting powders, PbI_2 and methylammonium iodide (MAI), separately on glass, then the achieved film thicknesses were measured using a Dektak surface profilometer. MAI was purchased from Oxford Photovoltaics and lead (II) iodide, ultradry 99.999% (metals basis), was purchased from Alfa Aesar. MAI and PbI_2 (500mg of each) were placed in separate crucibles, and the substrates were mounted on a rotating substrate holder to ensure that a uniform film was deposited. The temperature of the substrates was kept at 21°C throughout the deposition. The chamber was allowed to reach a high vacuum (10^{-6} mbar), before the PbI_2 and the MAI were heated to reach a deposition rate of $0.4 Å s^{-1}$. Once the deposition rate had stabilized along with the pressure (3×10^{-6} mbar), the substrates were exposed to the vapour. The rates of both MAI and PbI_2 deposition were monitored using a quartz crystal microbalance (QCM). The final deposition rate was 0.8 $Å s^{-1}$. The thickness of the samples was controlled by varying the exposure time of the substrates to the vapour. Thereafter the thicknesses of the films were accurately determined by using a Dektak surface profilometer, an FTIR transfer matrix method, and by capturing scanning electron microscopy images of the cross sections as detailed below.

2 Initial Material Characterisation

2.1 Scanning Electron Microscopy

2.1.1 Sample Preparation

Samples for scanning electron microscopy (SEM) were prepared on a quartz substrate as detailed above. All samples were cleaned using a nitrogen gun, and a sputter coater was used to deposit a 3 nm coating of platinum to improve conductivity. Carbon tape was applied to secure the samples and prevent charge build-up by further increasing the conductivity. Samples for cross-sectional SEM were cleaved in two halves, using a diamond scribe, before the deposition of the platinum.

2.1.2 Experimental Details and Results

A Hitachi S-4300 scanning electron microscope with an accelerating voltage of 3 KeV was used to capture cross-sectional and top view images of the samples, as shown in Figure S1. The top view images show a slight increase in the grain size with thickness, but this is a very weak trend, and the average grain size remains $\sim$100 nm. This demonstrates that each of the samples share a similar surface morphology, with no evidence of any significant trend with thickness. The large-scale images (Figures S1(h) & (i)) highlight the homogeneity of the films across several microns. This high degree of uniformity enables us to define a single film thickness across the full extent of the sample. This uniformity is further shown in the cross-sectional images displayed in Figures S1(j), (k) and (l), which confirm the consistency of the film thickness across the substrate.

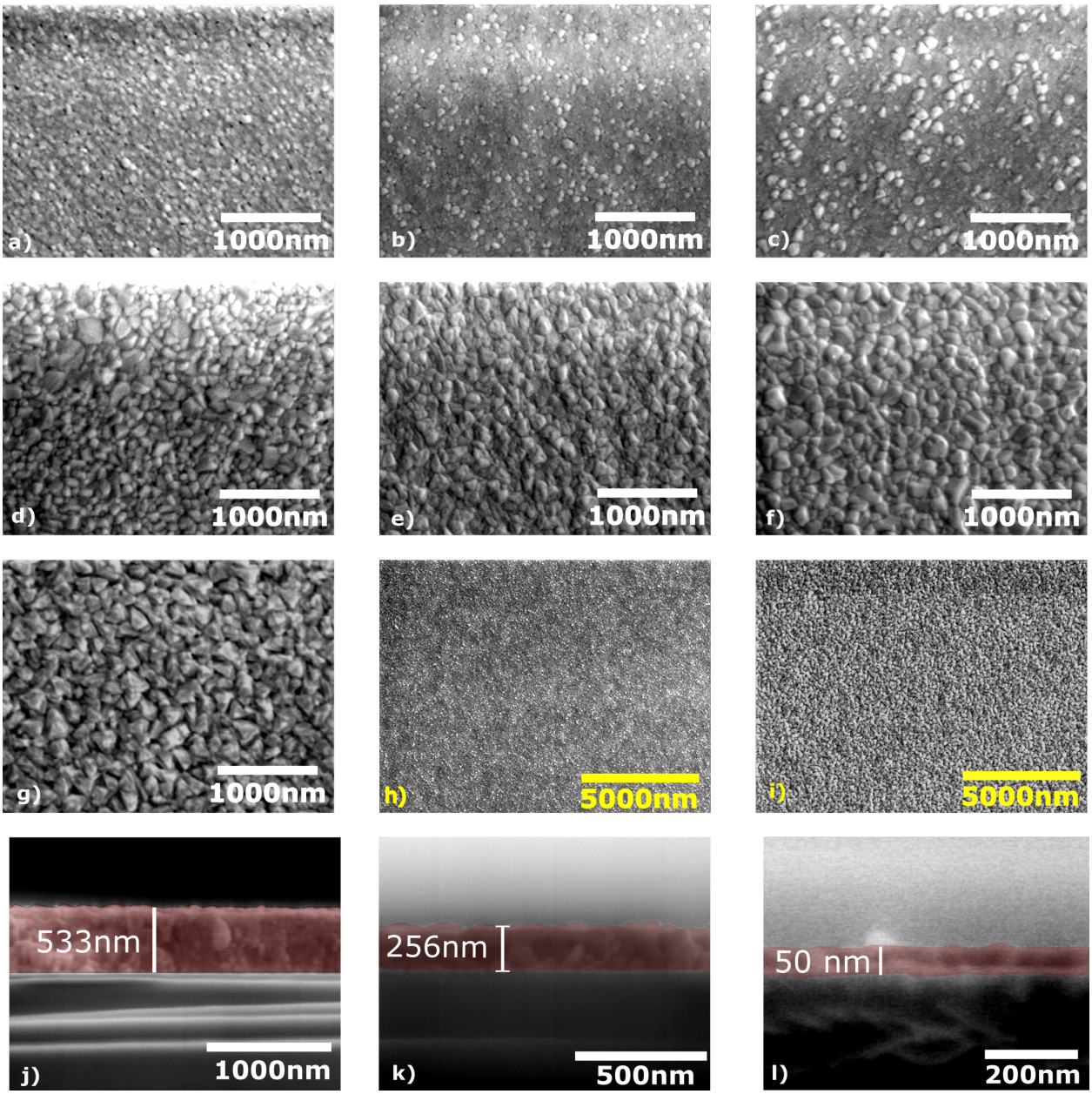

Figure S1: Scanning electron microscope images of samples showing $\times 35\,000$ magnification for films of thickness (a) 50 nm (b) 74 nm (c) 149 nm (d) 140 nm (e) 256 nm (f) 295 nm (g) 533 nm as well as $\times 8\,000$ magnification for (h) 50 nm and (i) 533 nm thick films. The images (j) - (l) show cross sectional images of films whose thickness is indicated by the labels.

2.2 Grazing Incidence Wide Angle X-Ray Scattering (GIWAXS)

Grazing-incidence wide angle X-ray scattering (GIWAXS) probes length scales in the crystallographic range. Random crystal orientation produces Debye-Scherrer rings with equal intensity distribution. For oriented samples higher intensities are visible depending on the orientation of the specific crystal plane. We conducted GIWAXS measurements at the beamline P03 of the German Electron-Synchrotron (DESY), Hamburg. The beam energy was 13 keV, the incident angle 0.4°and the sample-detector distance 279.6 mm. The raw detector images taken with a Pilatus 300k pixel detector are reduced and corrected with the software Igor Pro. For evaluation of crystal orientation we take five sector cuts and integrate the intensity over the azimuthal angle. The 2D GIWAXS patterns with corresponding sector cuts are shown in Figure S2, with the full treatment of the GIWAXS data being as previously reported.[S2,S3]

Some samples show a high degree of crystal orientation, e.g. for film thicknesses of 50 nm, 74 nm and 149 nm. The presence of the (220) reflex at two positions shows that two preferred orientations are present, respectively with the (002) and the (200) planes parallel to the substrate which is also apparent from different peak intensities in the sector cuts. Dominant is the (200) orientation. On the other hand, samples 140 nm and 295 nm do no show any preferred crystal orientations.

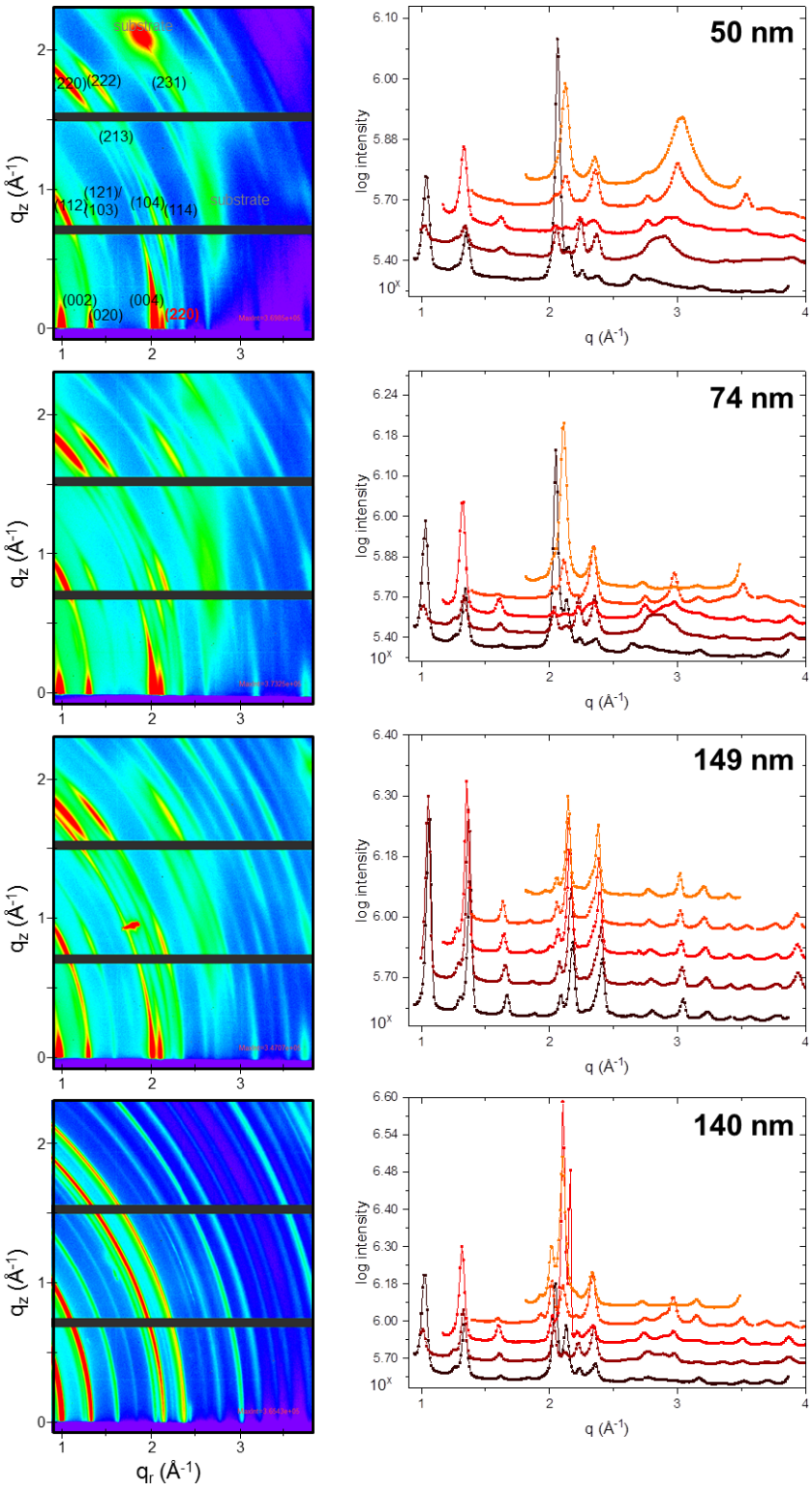
50 nm
74 nm
149 nm
140 nm
log intensity
q (Å-1)
qz (Å-1)
qr (Å-1)
substrate
(220)
(222)
(231)
(213)
(121)
(112)
(103)
(104)
(114)
(002)
(020)
(004)
(220)

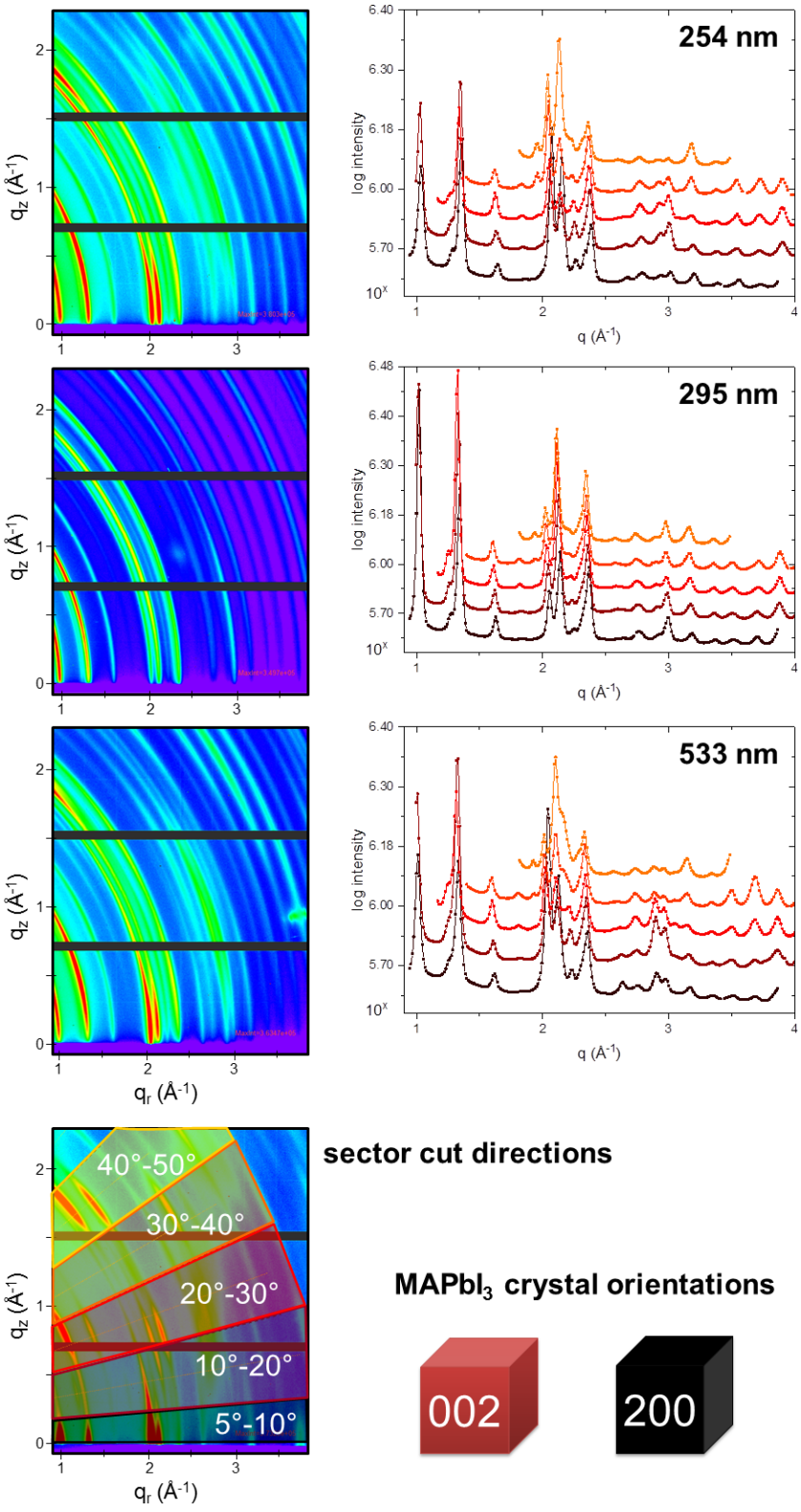

Figure S2: Grazing incidence wide angle x-ray scattering patterns and sector cuts for each sample. The results show slight variations in crystal orientation across the samples, however this does not follow any trend with thickness.

2.3 Photoluminescence Spectra

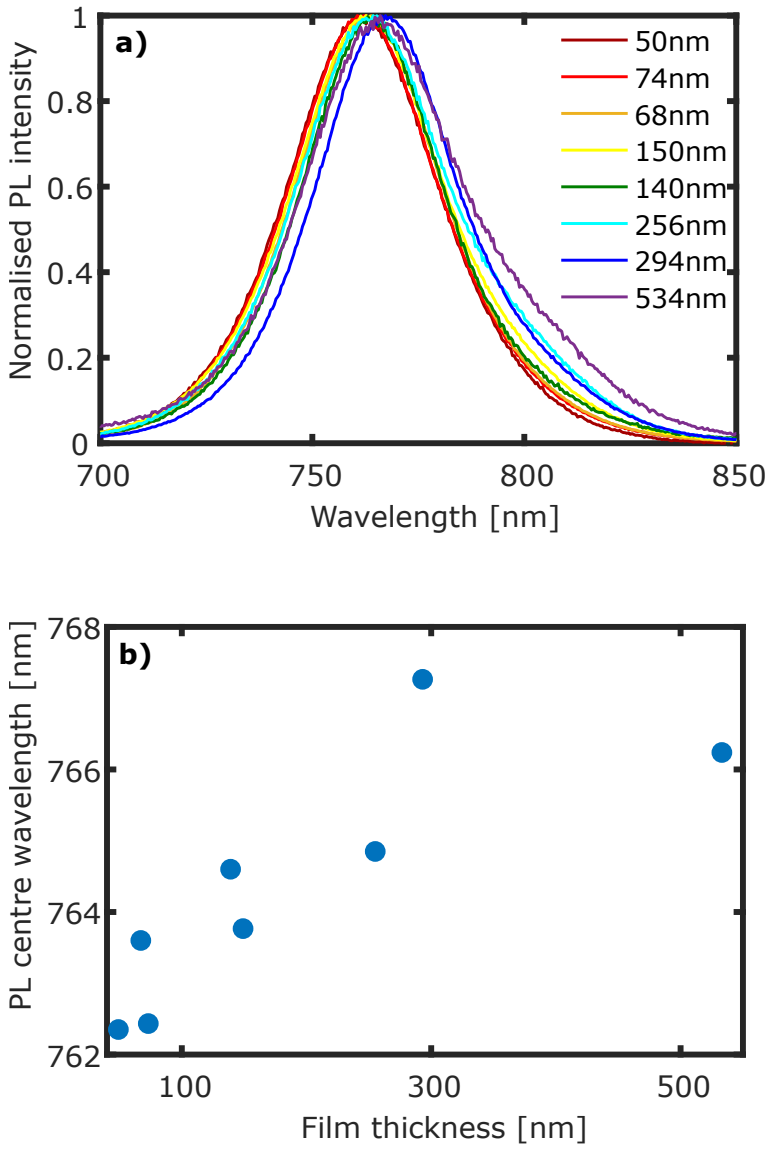

Figure S3: (a) Photoluminescence spectra obtained for each sample whose film thicknesses are indicated in the legend. Excitation was provided by a 400-nm picosecond pulsed laser diode (PicoHarp LDH-D-C-405M), and the emitted PL spectra was collected using a Princeton Instruments SP-2558 grating spectrometer and a PI-MAX4 Princeton Instruments iCCD. (b) Variation in centre wavelength of the PL spectra as a function of film thickness.

3 Calculation of Absorption Spectra

3.1 Experimental Details

Reflection and transmission spectra were measured using a Bruker 80v Fourier-transform infra-red spectrometer with a tungsten halogen lamp source, a CaF beamsplitter and a silicon diode detector. Data was collected from 8999 - 30000 cm^{-1} at a resolution of 1 cm^{-1}. A UV-protected sliver mirror from Thorlabs was used as the reflection reference and a transmission reference was measured using an empty sample holder. Using these references we determined R and T, which are the fractions of reflected and transmitted light for our samples.

3.2 FTIR Transfer Matrix Model

The complex refractive index, $N = n+i\kappa$, of each sample was determined using a generalised transfer matrix approach developed by Harbecke.[S4] The model determines the R and T from the combined film and substrate system, accounting for coherent multiple reflections within the perovskite layer (50-530 nm thick), and incoherent reflections from the quartz substrate (2 mm thick). As the reflections within the perovskite are coherent, the reflected and transmitted intensities are highly sensitive to the film thickness. This allows the model to be used to determine the thickness of the perovskite layer, as discussed below.

3.3 Extraction of Quartz Complex Refractive Index

The transfer matrix model was first used to extract the complex refractive index, N_{qu}, of the quartz substrate. By fitting the model to the experimentally obtained R and T for a blank quartz substrate, n_{qu} and κ_{qu} were extracted, as shown in Figure S4. The transfer matrix model fits the data well across the whole wavelength range, and the extracted value of refractive index is as expected for quartz. This value for N_{qu} was then used for the substrate when the properties of each perovskite layer were extracted.

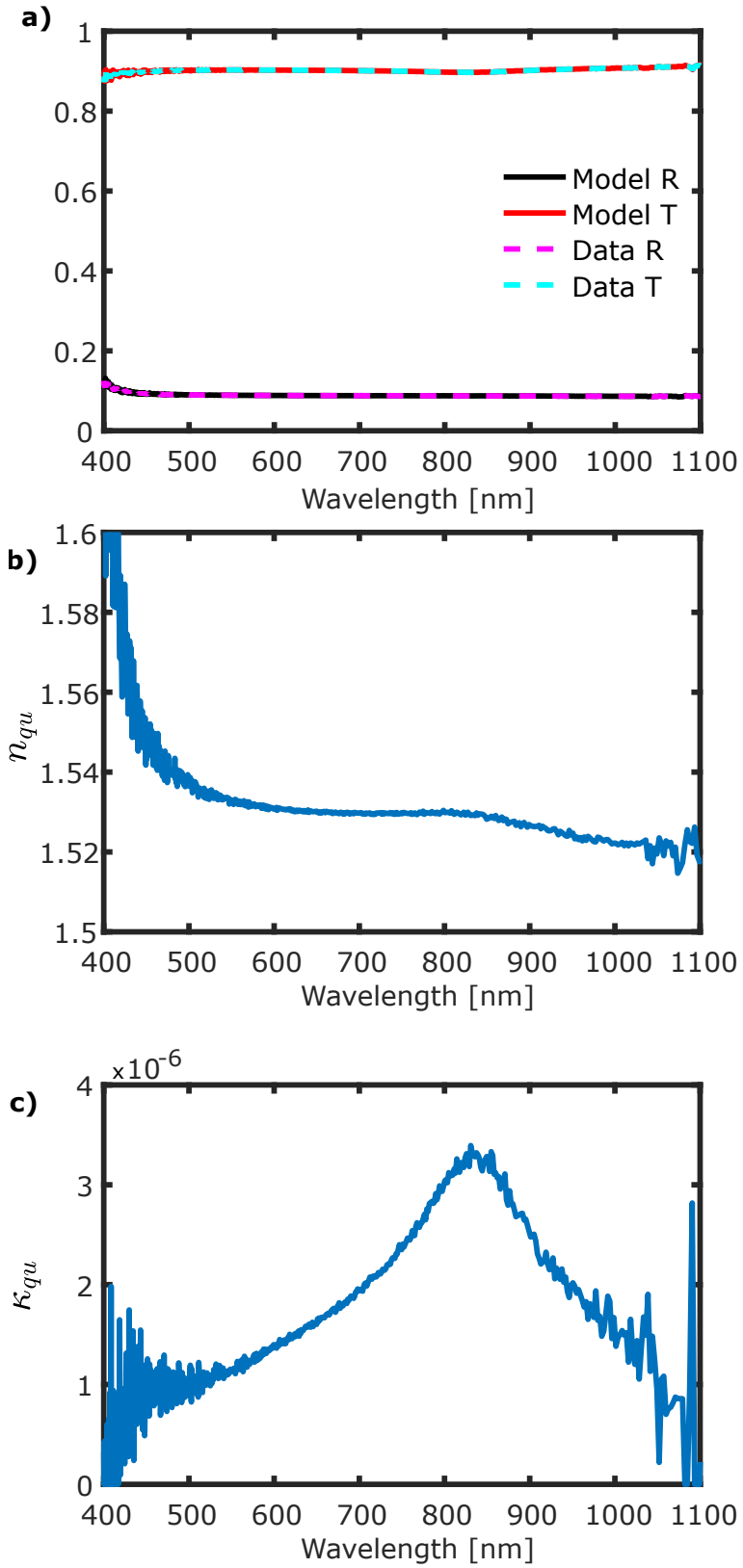

Figure S4: (a) Fits of transfer matrix model to the experimental R and T data for a blank quartz substrate. The real and imaginary parts of the extracted complex refractive index are shown in (b) and (c) respectively.

3.4 Extraction of Perovskite Complex Refractive Index

With the complex refractive index for the quartz substrate determined, the transfer matrix model was then applied to the perovskite layer. As the reflections within the perovskite layer are coherent, the model is highly sensitive to the film thickness. This means that both the thickness and complex refractive index N_{per} of each sample can be determined. Initial estimates of film thickness were obtained from a Dektak 150 surface profilometer, these values were then refined by the transfer matrix model, with the results shown in Table S1. Comparing the two measurements, there is a strong agreement between the DekTak and

Table S1: Perovskite film thickness for each sample as determined by determined by different methods

QCM Nominal thickness [nm]	45	60	110	150	220	300	400
Dektak profilometer thickness [nm]	60	80	152	144	274	310	540
Thickness from fits to FTIR data [nm]	**50**	**74**	**149**	**140**	**256**	**295**	**533**

transfer matrix model, both of which differ in several cases from the thickness predicted by the quartz crystal microbalance (QCM) during evaporation. The values determined by the DekTak and transfer matrix model are also in agreement with the SEM cross-sections in Section S2, suggesting the error is in the QCM prediction. The QCM thickness estimates provide only a rough guide to film thickness based on the evaporation protocol for a 300-nm thick film, so it acceptable that this should disagree with the actual direct measurements of film thickness. Throughout this study we take the sample thickness to be that extracted by our FTIR transfer matrix model (shown in bold in Table S1) as this is the method most sensitive to the sample thickness.

The fits of the transfer matrix model to the experimental R and T values for each sample are shown in Figure S5, where it can be seen that the model provides a good fit to the data. For the model to accurately fit the data, it is important that the thickness is highly uniform, as a variation in sample thickness will result in a range of interference patterns in the overall sample R and T. Therefore, the close agreement between the data and the transfer matrix model highlights the highly planar nature of these vapour-deposited samples. The samples also display minimal scattering as shown by the very weak absorption below the bandgap, discussed further in Section 3.6.

Figure S6 shows the extracted values of κ_{per} and n_{per} for each sample, as well as the average of the entire sample set. Our samples all have very similar refractive indices and absorption coefficients, α, showing that the absorption coefficient spectra of the samples display no dependence on film thickness. At shorter wavelengths, the thicker films do not transmit sufficient light, making the extraction of the refractive index less accurate, however,

to model self-absorption we only require a knowledge of N_{per} at the PL wavelengths.

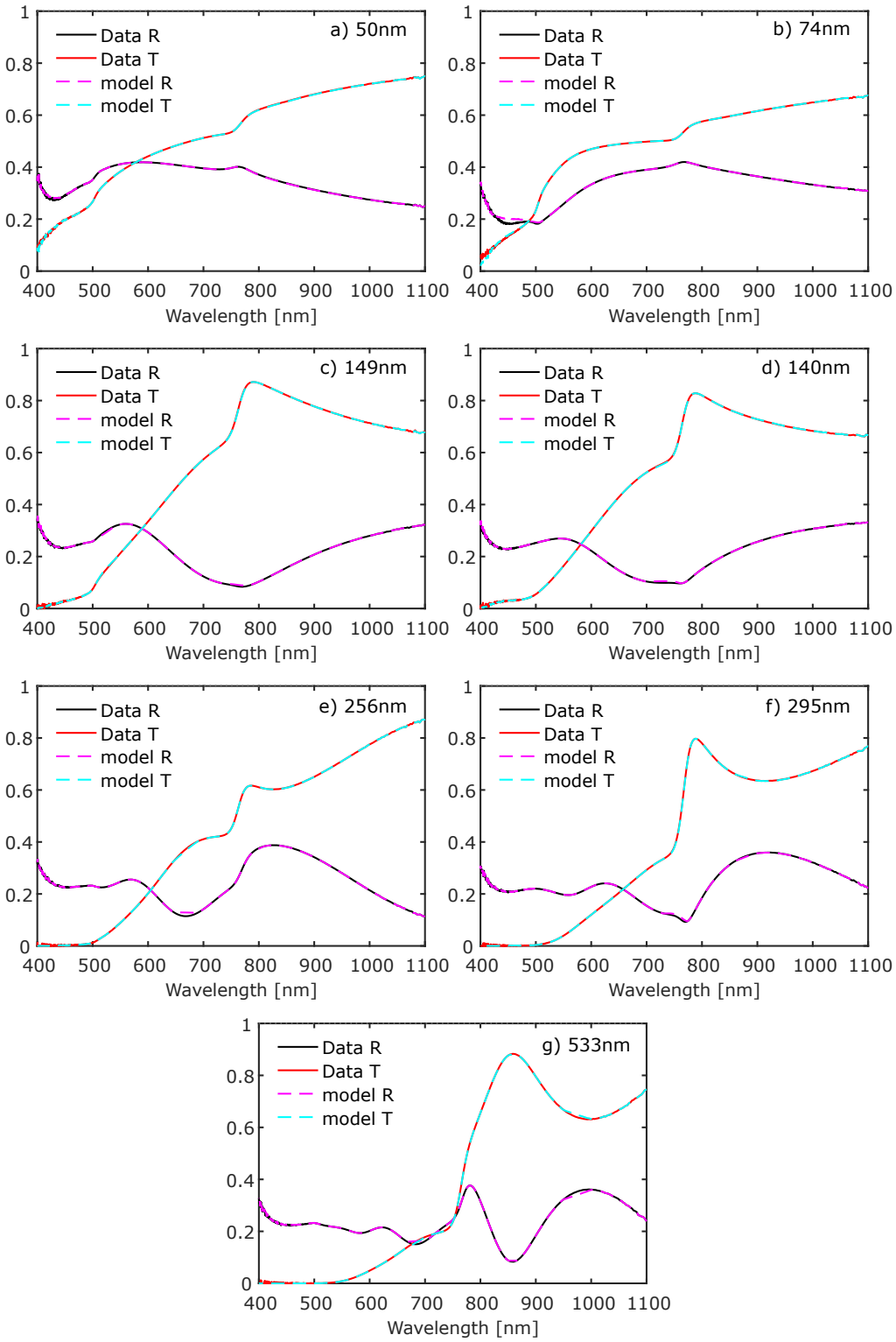

Figure S5: Individual fits of the transfer matrix model to the experimentally measured R and T of each sample.

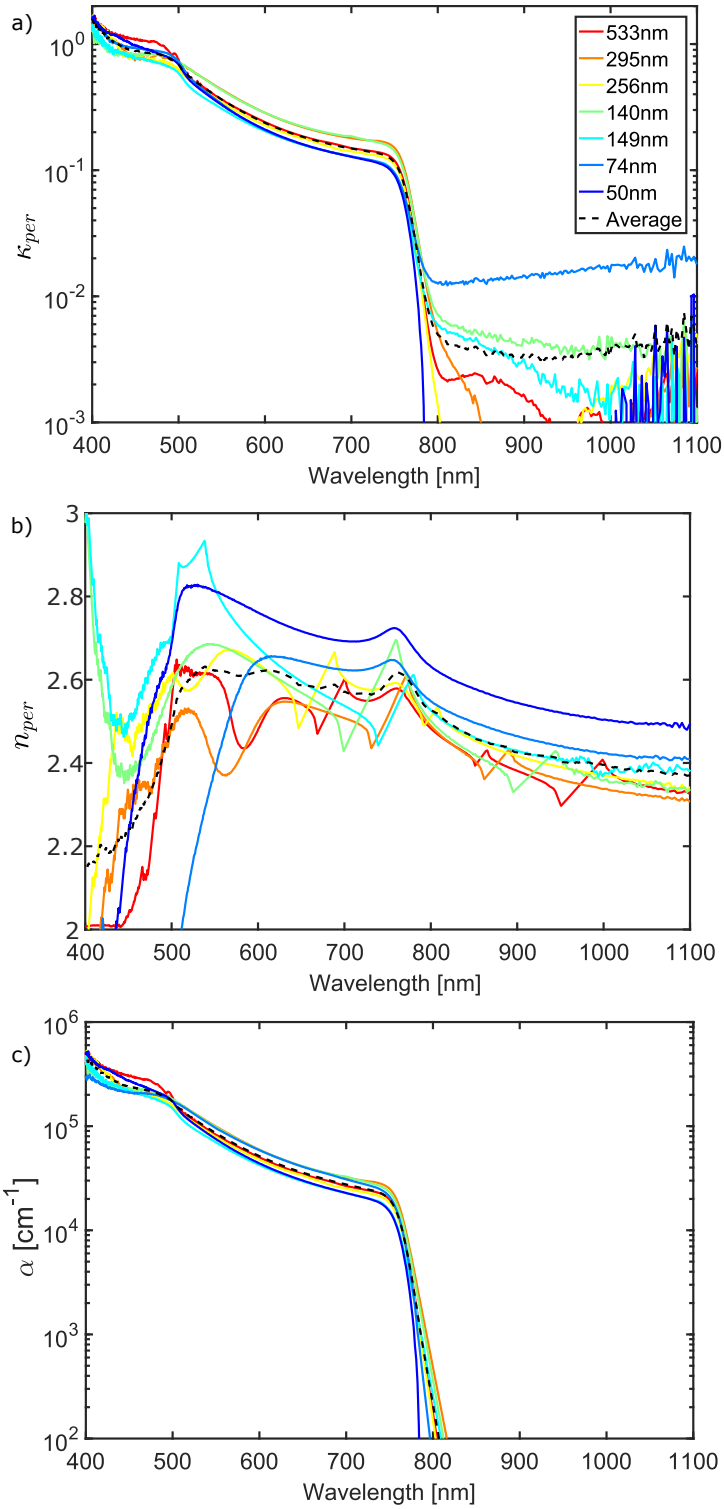

Figure S6: Extracted parameters for the complex refractive index of each of the perovskite samples using a transfer matrix model. (a) and (b) show the imaginary and real elements of the refractive index as directly extracted from the model. (c) shows the absorption coefficient, $\alpha = (4\pi\kappa)/\lambda$, corrected for scattering, as discussed in Section 3.6.

3.5 Comparison of Methods Used to Extract Absorption Coefficient

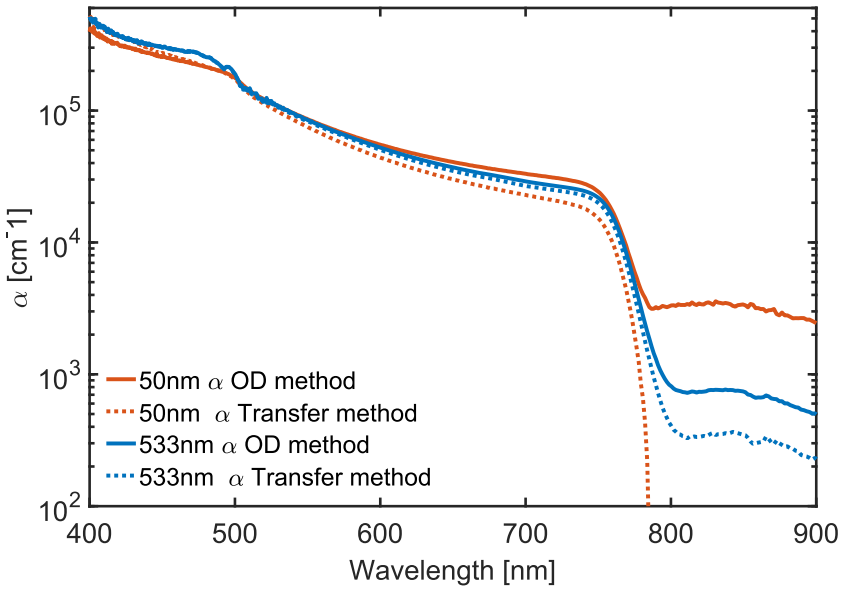

Figure S7: Comparison of absorption coefficient spectrum extracted using our transfer matrix approach to that produced by using the optical density method of Equation S1, for both a thick and a thin film. All data are shown without correction for scattering.

The absorption coefficient, α, of the perovskite samples has been calculated here using a transfer matrix method, but another common technique is to determine α from the optical density (OD). This approach uses Beer's law and the fractions of light transmitted and reflected by the sample to obtain:

$$\alpha = -\frac{1}{d}\ln(\frac{T}{1-R}), \tag{S1}$$

where d is the film thickness. Figure S7 compares the raw value of α determined by each approach, before any corrections are applied. It can be seen that the two methods produce a very similar absorption spectrum, however, there are some differences, particularly at the absorption edge where the transfer matrix method provides a clearer rise in α. One reason for this disagreement is that the OD method produces an effective α for the combined perovskite and substrate stack, whereas the transfer matrix method accounts for the effect of the substrate and isolates the absorption of the perovskite layer. When the absorption of the perovskite is strong, very little light is transmitted through the film and there is little effect from the substrate. However, at the absorption edge, or in thinner films, the absorption is weaker and multiple reflections from the substrate are more significant. This leads to the

differences in the absorption spectra produced by each approach, shown in Figure S7, which are most clearly seen in the 50 nm film. For this reason, the transfer matrix method is employed in this study to decouple the effect of the substrate from that of the film, and obtain α, independent of any substrate effects.

3.6 Correction of Absorption Data for Scattering

The raw absorption data in Figure S6(a) contains contributions from both scattering and absorption, as the FTIR could only detect coherent transmission or reflection from a sample. This means scattered light will not be detected, and is not directly distinguished from actual absorption. As this light is not actually absorbed by the perovskite to produce charge-carriers, it is important to differentiate scattering and absorption when modelling self-absorption.

The two processes are separated by assuming that the absorption below the bandgap arises only from scattering, and taking the average α in this region to be the strength of scattering in the sample. The samples all displayed very low levels of scattering, occurring on a length scale of $1/\alpha_{scatter} \approx 20\,\mu$m for the most strongly scattering sample, much longer than the absorption lengths of a few hundred nanometers typical for the PL. In relation to our ray tracing model (Section 6) this means that most of the self-absorption takes place on a length scale where scattering can be discounted, however, we use the scattering length scale of $20\,\mu$m as an upper limit on the coherent propagation distance of PL within the samples.

To extract a scattering-corrected absorption spectrum, the average scattering amplitude was first subtracted from the raw absorption spectrum, before the absorption onset was exponentially attenuated to zero. This process produces the corrected α (Figure S6(c)), which are then used in the ray tracing model, described in Section 6.

4 THz Spectroscopy

4.1 OPTP Experimental Details

Optical-Pump THz-Probe (OPTP) measurements were performed using a Spectra Physics Mai Tai-Empower-Spitfire Pro Ti:Sapphire regenerative amplifier. The amplifier generated 40-fs pulses with a centre wavelength of 800 nm at a repetition rate of 1.1 kHz. The optical pump excitation was generated by frequency doubling the input pulse using a beta barium borate crystal to give a pump pulse with a centre wavelength of 400 nm. THz probe pulses were generated by optical rectification in a 450 μm (110)-GaP crystal and detected using electro-optic sampling in a ZnTe crystal (composed of 0.2 mm (110)-ZnTe on 3 mm (100)-ZnTe). The FWHMs of the beams for the pump and THz pulses at the sample were measured to be 3.9 mm and 1.4 mm respectively. The sample, THz emitter and THz detector were held under vacuum of 10^{-2} bar during the measurements.

4.2 Extraction of THz Charge-Carrier Mobility

The THz mobility is determined using the method described by Wehrenfennig et al.[S5] In brief, the sheet photo-conductivity, ΔS, of a material with a thickness much less than the wavelength of the THz radiation can be expressed as

$$\Delta S = -\epsilon_0 c(n_a + n_b)(\frac{\Delta T}{T}) \tag{S2}$$

where n_a and n_b are the THz refractive indices of the materials interfacing the perovskite layer at the front and rear respectively. The quantity $\Delta T/T$ is the ratio of the photo-induced change in THz electric field to the transmitted THz electric field in the dark. The initial number of photo-excited charge carriers N is given by

$$N = \phi\frac{E\lambda}{hc}(1 - R_{pump})(1 - T_{pump}) \tag{S3}$$

with E being incident pump pulse energy, λ the excitation wavelength, ϕ the ratio of free charges created per photon absorbed, and R_{pump} and T_{pump} being the reflected and transmitted fractions of the pump beam. These two equations can be used to extract the charge carrier mobility μ through

$$\mu = \frac{\Delta S A_{eff}}{Ne} \tag{S4}$$

where A_{eff} is the effective area from the overlap of the pump and probe beams and e is the elementary charge. Substituting Equations S2 and S3 into Equation S4 we obtain

$$\phi\mu = -\frac{\epsilon_0 c(n_a + n_b)(A_{eff})}{Ne\lambda(1 - R_{pump})(1 - T_{pump})}(\frac{\Delta T}{T}) \tag{S5}$$

from which the effective charge-carrier mobility $\phi\mu$ may be determined based on the pump beam parameters and the initial measured $\Delta T/T$ of the sample. Here, μ is the charge-carrier mobility, and ϕ is the charge-to-photon branching ration which is assumed to be unity at room temperature for $MAPbI_3$. The charge-carrier mobility of each sample was extracted by exciting the sample at a number of different excitation fluences, and making a linear fit between N and the initial $\Delta T/T$. The excitation fluences were all sufficiently low (< 50 μJ cm^{-2}) in order to avoid non-linear effects such as two-photon absorption. The charge carrier mobility as a function of thickness is shown in Figure S8 where it can be seen that although there is a spread in values, there is no systematic variation with film thickness.

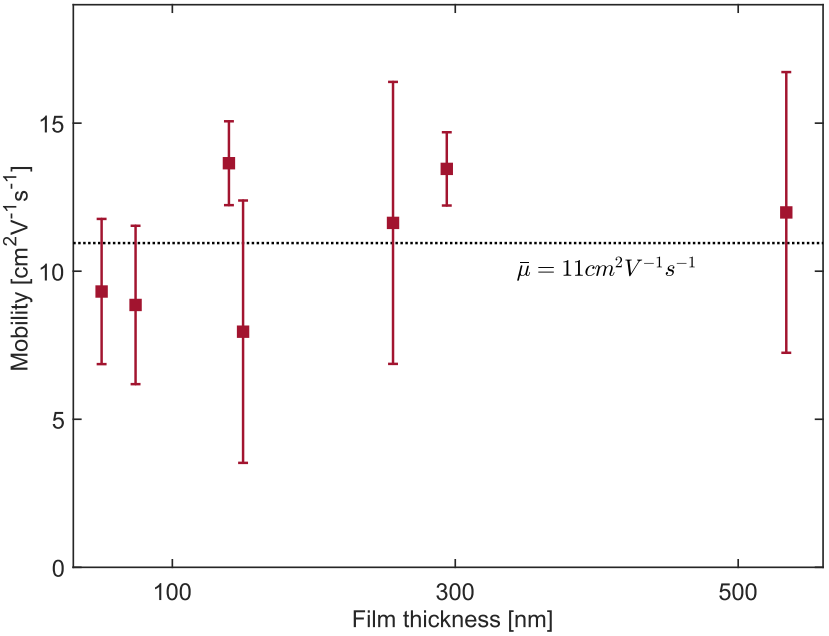

Figure S8: Charge-carrier mobility shown against perovskite film thickness determined using OPTP spectroscopy as described in the text.

5 Modelling Charge-Carrier Recombination

Modelling of the charge-carrier recombination dynamics requires knowledge of the initial distribution of charge-carriers and a kinetic model for their dynamics. Here we present a full explanation of the two models which are used in our study, as well as different approaches for describing the initial charge-carrier distribution.

5.1 Charge-Carrier Density Profiles

The initial charge-carrier distribution in a perovskite film can be modelled either by assuming a single charge-carrier density in the excited sample volume or accounting for a variation in charge-carrier density throughout the bulk of the sample. In all cases, the areal extent of the volume is given by the effective area, A_{eff}, which is determined by the overlap of the pump and probe beams. The area excited by the pump beam is much larger than that excited by the probe beam, with the two having FWHMs of 3.9 mm and 1.4 mm, respectively. This means that there will be no change in the charge-carrier density across the area of the probe beam.

However, there will be a change in the charge-carrier density (n) through the depth of the film, due to the attenuation of the pump as it passes through the perovskite film. The simplest way to model the charge-carrier distribution formed by the pump beam is to assume that all charge carriers are absorbed within $1/\alpha_{pump}$ of the surface, and that there exists a single n within this volume. We term this type of n profile a 'step profile', as when viewed in profile, there is a sharply defined step in n as shown in Figure S9. Another similar charge-carrier profile is to assume that the charge-carriers will be evenly spread throughout the entire film thickness, giving the 'flat profile' in Figure S9. These two profiles are computationally simple as they have only a single n, however, this also makes them somewhat unphysical, as in reality there will usually be a range of values of n throughout the sample. The flat profile is used in figure 3a of the main text, as in that case the n distribution being described is assumed to be evenly spread across the film. However, these profiles are not used in our main results when describing pump-probe experiments but are employed only in our comparison of modelling approaches in Section 7, where they are also discussed further.

The initial n profile in the sample can be more accurately modelled by including multiple charge-carrier densities, using Beer's law to determine the n profile. Beer's law states that the intensity, I, of the pump beam travelling through the perovskite will decay in intensity according to

$$I(z) = I(0)e^{-\alpha z} \tag{S6}$$

where z represents distance travelled through the perovskite. As the pump beam attenuates exponentially through the film, it will generate an exponentially attenuating charge-carrier profile, shown in Figure S9. To model this we use a 'Beer profile', in which the film is split into 2 nm slices, which each have a different n determined by Equation S6. This type of profile more accurately reflects the initial n profile through the film, but is computationally more intensive. As such, the Beer profile is used throughout our main results whenever the 'Standard Model' (see below) is employed. To reconstruct the response of the sample, the photo-conductivity decays within each of the slices is summed to give the overall photo-conductivity transient. The effect of using these different profiles on the values determined for the recombination constants is considered in Section 7.1

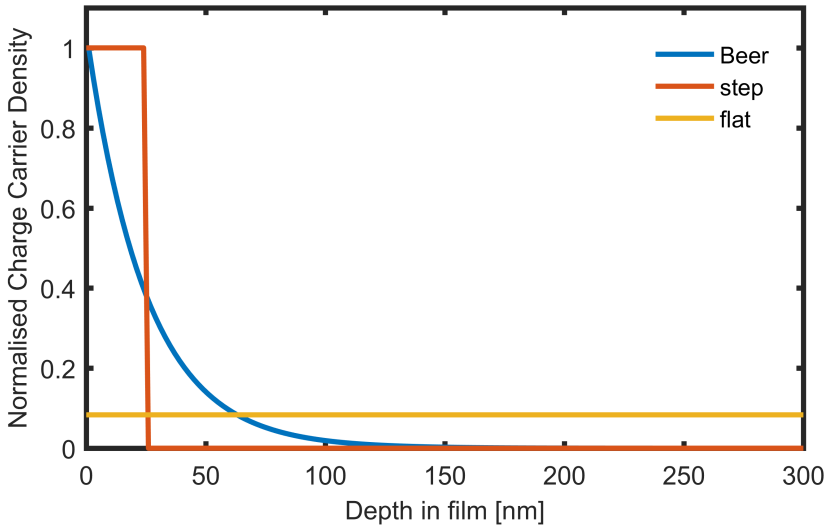

Figure S9: Modelled representation of the various n profiles used in our study, with each profile normalised to show the same number of charge-carriers.

5.2 Standard Model For Charge-Carrier Recombination Dynamics

We initially use a Standard Model to fit the charge carrier dynamics in our samples. This model is widely used in other studies,[S6,S7] and ignores the effects of self-absorption and charge-carrier diffusion.

The free charge-carrier recombination within this Standard Model is governed by the rate equation:

$$\frac{dn}{dt} = G - k_3 n^3 - k_2^{\text{apparent}} n^2 - k_1 n \tag{S7}$$

where n is the charge carrier density, G is the charge-density generation rate. k_1, k_2^{apparent} and k_3 are the first, second and third order recombination constants respectively.

Equation S7 is first solved in terms of the experimentally observed quantity $x = \Delta T/T$, the photoinduced change in THz transmission:

$$\frac{dx}{dt} = G - A_3x^3 - A_2x^2 - A_1x \tag{S8}$$

to determine the A coefficients. These A coefficients relate linearly to the recombination constants due to the directly proportional relation between n and x, with each pair being related by:

$$A_i = C^{i-1}\phi^{i-1}k_i. \tag{S9}$$

The proportionality factor, C, which links the absorbed photon density and the initial THz response is defined:

$$C = \frac{E\lambda}{hc \times V \times x(0)}(1 - R_{pump})(1 - T_{pump}), \tag{S10}$$

where V is the volume in which the charge carriers are contained. It is this direct dependence of the apparent bimolecular charge-carrier recombination constant k_2^{apparent} upon the volume occupied by the charge-carriers which makes the choice of charge-carrier profile in the sample so crucial.

5.3 Self-Absorption Model For Charge-Carrier Recombination Dynamics

The second model used to understand the charge-carrier dynamics is the 'Self-Absorption' Model which, unlike the Standard Model above, accounts for self-absorption of the emitted PL and charge-carrier diffusion. With the inclusion of the extra terms for charge diffusion and photon re-absorption, the governing equation for the charge-carrier dynamics is now:

$$\frac{\partial n}{\partial t} = D\frac{\partial^2 n}{\partial z^2} + G - k_3n^3 - k_2^{\text{intrinsic}}n^2 - k_1n \tag{S11}$$

where the first term accounts for charge-carrier diffusion and the second term is the charge-carrier generation rate, which accounts for photon re-absorption. The coefficient D is the diffusion constant, which can be determined using the Einstein relation:

$$D = \frac{\mu k_b T}{e} \tag{S12}$$

using the previously determined charge-carrier mobility for each sample as appropriate. For our modelling we use the average value of μ ($11\,cm^2/Vs$), from which we obtain $D = 0.3\,cm^2/s$. In order to solve Equation S11, the perovskite film is split into 2-nm thick

slices and a finite difference time domain method is used. The diffusion term requires very small time-steps of 50 fs, but the other terms are only updated at 1-ps intervals. The model works by first allowing n at each point in the film to evolve for 1 ps under diffusion, using a forward Euler method. Diffusion is restricted to 1D only, as on the time-scale of our OPTP experiment diffusion parallel to the film surface will not be significant. At the end of each ps time-step the charge-carrier decay is calculated, so that n at each point in the model can be updated. From the calculated amount of radiative bimolecular recombination events, the number of photons produced at each point in the film is determined, and using the ray tracing model (described in Section 6) these photons are then either self-absorbed or lost. This process is repeated for total time period of 2500 ps, to cover the full range of our OPTP experiment. The total $\Delta T/T$ of the sample is then determined using Equations S2 and S4, with the total number of charge-carriers at each time-step being given by the sum of the charge-carriers across all of the slices.

5.4 Global Fits to Photoconductivity Transients

The intrinsic bimolecular recombination constant $k_2^{\text{intrinsic}}$ was determined by global fits of our models of charge-carrier dynamics to photo-conductivity decays collected for a range of excitation fluences. The monomolecular decay was too slow to be noticeable within the 2.5-ns time window of our experiment, and so was fixed at 10^{-7} s^{-1}. Additionally, from the modelling in Section 7 it was determined that the fluences used were too low to result in noticeable contributions from Auger recombination, so k_3 was also fixed at zero. A set of photo-conductivity decays with a range of fluences were simultaneously fitted to provide an optimised value of $k_2^{\text{intrinsic}}$ for each sample, using the Self-Absorption Model. The fits associated with the Self-Absorption Model to the photo-conductivity transients of each sample are shown in Figure S10. Also shown is the variation in $k_2^{\text{intrinsic}}$ with film thickness, as determined by the Self-Absorption Model.

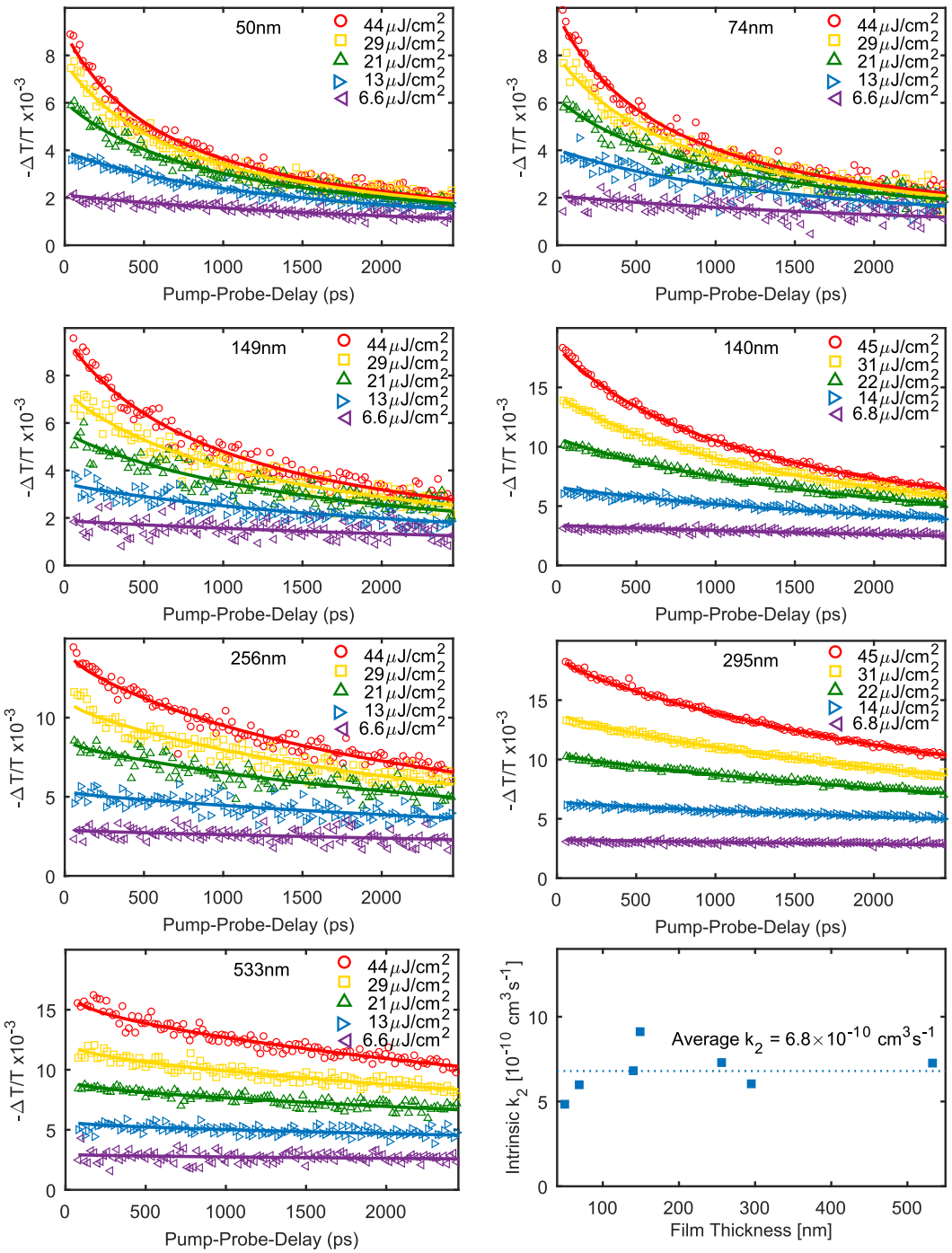

Figure S10: THz photoconductivity transients for samples of different thickness as indicated in the figure panels shown together with global fits for all fluences based on our Self-Absorption Model. Also shown is the trend in intrinsic value of the extracted bimolecular recombination constant $k_2^{\text{intrinsic}}$ across the thickness range, showing a single, average value as indicated.

6 Ray Tracing Model Used For Self-Absorption Model

6.1 Description of Ray Tracing Model

Self-absorption is accounted for using an explicit ray tracing model, which determines the amount of emitted PL that is reabsorbed at each point in the film. The model separates the perovskite film into a stack of 2 nm slices which can either emit or absorb PL. Propagation of PL from a given slice is simulated, using Beer's law to determine how much PL is re-absorbed in each of the other slices. Reflections at the film boundaries are assumed to be coherent, and are governed by Fresnel equations. If the PL is not self-absorbed, its propagation distance will be limited by scattering and so based on our estimation of scattering strength in Section 3.6, propagation of photons is modelled for 20 μm. After this distance any remaining PL is considered lost to scattering and unabsorbed. This propagation distance is much less than the size of the area excited by the pump, and so any self-absorption from propagation of photons parallel to the film surface will be cancelled out by the similar propagation from the surrounding regions. For this reason the propagation can be restricted to 1D through the sample thickness, however, the emission angle still affects self-absorption, as it determines the distance PL must travel through each 2 nm slice and the strength of reflections at the boundaries. Using this ray tracing procedure, the fraction of PL emitted from a given slice, at a particular emission angle and wavelength, which ends up being absorbed by each other slice can be determined.

Within our samples the emission of PL will be isotropic, and across a range of emission wavelengths. For each slice in the film, isotropic PL emission can be modelled by appropriately averaging the results of the ray tracing model over all possible angles. This determines where the PL emitted isotropically, from one slice, at a given frequency will be re-absorbed. Repeating this procedure for each slice provides a monochromatic 'map' of where the PL emitted by each slice will end up being re-absorbed. This information can then be represented as a matrix which reallocates the PL emitted by bimolecular recombination in each slice to the appropriate absorbing slices. We repeated this process for each wavelength from 651-830 nm, using the relevant absorption coefficient to produce a series of monochromatic PL re-absorption maps.

6.2 Relation of Emitted and Measured PL Spectra

In order to accurately model self-absorption, the monochromatic PL reallocation maps from the previous section must be combined with weights based on the emitted PL spectrum. However, the externally measured PL spectra are subject to self-absorption, so it is necessary

to correct for this and determine the PL spectrum as emitted within the material. The externally measured PL spectra collected for each of our samples are shown in Figure(S3)b, where a clear red-shift in the centre wavelength of the emitted PL with increasing film thickness can be observed. This red-shift arises because PL typically has to travel further to escape thicker films, meaning the shorter wavelength components will be attenuated more strongly, and the external PL peak is red-shifted.

As the ray tracing model predicts how much of the emitted PL at a given frequency will escape the perovskite film to be measured as PL, we can reverse the model to reconstruct the emitted PL spectrum. The results of this correction are shown in Figure S11, where the spread in the externally measured PL centres is visibly reduced in the corrected emitted spectra, as the shorter wavelengths are recovered. Neglecting the red-shift of emitted PL would lead to an underestimate of the effects of re-absorption, so this corrected spectrum is used in generating the overall PL reallocation maps used in the previous section.

With the internal PL spectrum determined, the monochromatic PL reallocation maps described above can then be combined together with the appropriate weighting to provide a comprehensive PL reallocation map for a given sample.

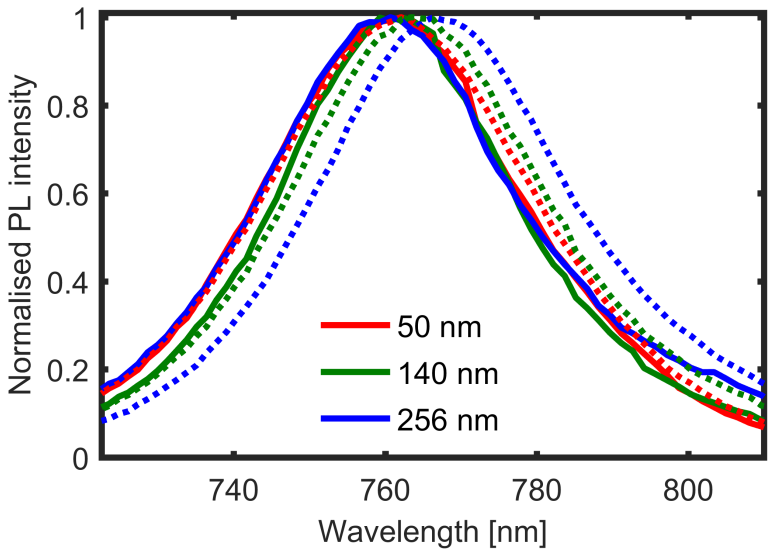

Figure S11: The dashed lines show the externally measured PL spectra for each of the labelled samples, while the solid lines show the PL spectrum as emitted within the sample, as extracted by our ray tracing procedure.

6.3 Creation of PL Reallocation Maps for Modelling

The PL reallocation maps produced for our samples are specific to the PL spectrum and absorption profile of each sample, however, the same approach can be used to model self-absorption in other systems. For the modelling in Section 7 and in the main manuscript, a set of PL reallocation maps were produced for a range of film thickness between 40 and 540 nm, using a common absorption profile and PL spectrum. These PL reallocation maps assume the perovskite film is bordered on one side by vacuum (refractive index 1) and on the other side a by quartz substrate (refractive index 1.55). This allows the comparison of the charge-carrier dynamics within identical model perovskite films, independent of any sample to sample variation, differing only in film thickness.

Additionally, PL reallocation maps were produced for a perovskite film between interfacing media with different refractive indices, to investigate the effect of out-coupling on PL re-absorption and charge-carrier recombination. These maps are used in Figures 2 and 3 of the main manuscript, and are based on 20 μm photon propagation in a 300nm thick perovskite film located between two semi-infinite media.

7 Quantitative Relations Between Different Models of Charge-Carrier Recombination

In Section 5 several possible methods of modelling the charge-carrier recombination dynamics in perovskite films were described, here we evaluate how the choice of model influences the value of the extracted recombination constants. In particular, quantitative relationships between the different models are established and it is illustrated how a less appropriate model can produce unphysical recombination coefficients.

We focus on the two models presented in Section 5; the Standard Model (widely used in literature) and the Self-Absorption Model (developed here). Additionally, two approaches to modelling the spatial distribution of n within the film have been highlighted, with either a single average charge-carrier density (the 'step profile') or a Beer ('Beer profile') distribution, incorporating several different charge-carrier densities, being used (Section 5.1).

To quantitatively compare these different methods for modelling charge-carrier dynamics, we follow the same approach as in our OPTP experiment. One model is used to produce a set of photo-conductivity decays, across a range of simulated pump fluences and these photo-conductivity decays are then fitted by a second model which determines an apparent value of k_2. This approach allows a high degree of control, as the recombination parameters in the first model (here referred to as $k_2^{\text{intrinsic}}$ and $k_3^{\text{intrinsic}}$) can be controlled and the relation between the two models evaluated across a wide range of parameters. As a means of comparing the $k_2^{\text{intrinsic}}$, which is used in the model generating the decay, with the k_2^{apparent} determined by the global fitting of the second model, the ratio

$$\Phi_2 = \frac{k_2^{\text{apparent}}}{k_2^{\text{intrinsic}}}. \tag{S13}$$

is defined. From monitoring the value of Φ_2 as $k_2^{\text{intrinsic}}$ is changed, it can be determined if a constant relation between the two models exists. If the value of Φ_2 is constant across a range of $k_2^{\text{intrinsic}}$, then this relation between the two models can be used to determine an unknown $k_2^{\text{intrinsic}}$ from k_2^{apparent}. This is important as, using such a relation, our Self-Absorption Model can be applied to previous studies which have used the Standard Model. In this section we investigate the circumstances in which such a relationship can be established.

7.1 Relating Charge-Carrier Density Profiles Within Standard Model

Before investigating the relation between our new Self-Absorption Model and the existing Standard Model, we first demonstrate how the use of different charge-carrier density profiles affect the perceived value of k_2. This is important, as while many studies have assumed a single average n,[S6,S7] others have accounted for multiple values of n present across different parts of the sample.[S8,S9]

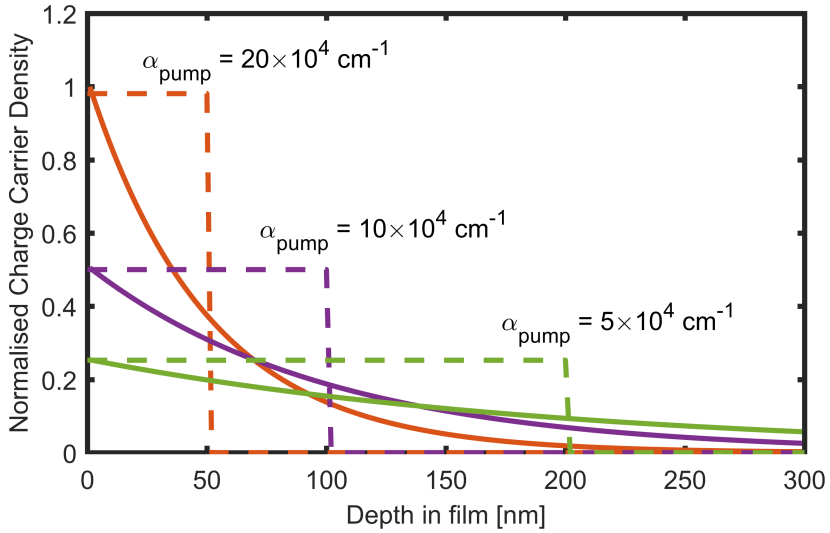

Figure S12: Modelled charge-carrier density n profiles in a 300-nm perovskite film on glass shown for different values of pump absorption coefficient. For each case, both the step profile (in dashed lines) and Beer profile (in solid lines) are shown.

The two n profiles which we shall compare are the 'step' and 'Beer' profiles, as shown in Figure S12. The two profiles are compared as described above: the Beer profile is used to create a set of photo-conductivity transients which the step profile then fits. Throughout this comparison, the underlying model for charge-carrier recombination remains the Standard Model, the only difference is in the assumed initial distribution of charge-carriers.

The determined relation between the two models is shown in Figure S13, for a range of absorption coefficients and film thickness. In this case Φ_2 is the ratio of k_2 as determined by the step profile to that used in the Beer profile, which generates the decay. Where the film thickness is larger than the absorption length of the pump, $\Phi_2 < 1$, meaning that k_2 determined using the step profile is smaller than that predicted when using the Beer profile. This can be understood from the fact that charge-carriers are more spread out in the Beer profile, and so are at a lower charge carrier density, therefore, to produce the same rate of charge-carrier decay the recombination constant must be larger. in this case, as the

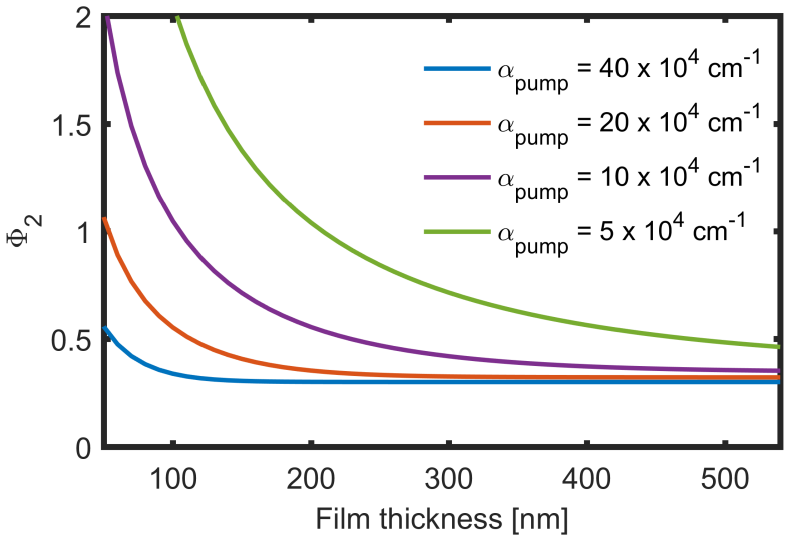

Figure S13: a) Φ_2 determined by fitting modelled photo-conductivity transients from an initial Beer n profile using a flat n profile, both with a Standard Model, for several different pump absorption coefficients. The Beer model used the recombination constants $k_2 = 6.4 \times 10^{-10}$ cm$^3 s^{-1}$ and $k_3 = 10 \times 10^{-30}$ cm$^6 s^{-1}$. The fits had k_3 fixed at 0, as the pump excitation fluences used were the same as in the experiment and Auger recombination was minimal.

absorption length of the pump increases, Φ_2 becomes closer to 1 as the average n used in the step profile becomes a better approximation of the Beer profile (demonstrated in Figure S12).

It should be noted that where the film thickness is less than the absorption length, applying the step profile is unphysical, as the charge-carrier density distribution assumed by the step profile extends further than the film boundary. In this case $\Phi_2 > 1$ with the n predicted by the step profile being lower than that found in the Beer profile. As the step profile is no longer appropriate in this case, it should only be used where the film thickness is greater than the absorption length.

We can also consider how the two profiles interpret various aspects of the photo-conductivity decay, as although both profiles can fit the same photo-conductivity decays, they each explain the decays using a different balance of charge-carrier recombination processes. At higher fluences there are two features to the photo-conductivity transients: an initial fast decay process, followed by a slower decay. When using the step profile, these decay components are interpreted as Auger and bimolecular recombination respectively. On the other hand, when using the Beer profile, all of this decay is interpreted as bimolecular. The region of high n at the front of the film results in fast initial recombination, while the low n region deeper in the film decays more slowly. If the Beer profile is taken to be a more accurate

representation of the n profile within the film this means that using the simpler step profile can result in an underestimate of k_2 and an overestimate of k_3. This relationship between the profiles is important and Φ_2 between the two cases is stable across a wide range of k_2 values. However, while this demonstrates the value of this comparison method, it is of more practical interest to now relate the Standard and Self-Absorption Models.

7.2 Relating Standard and Self-Absorption Models in the Equilibrium Case

The simplest scenario in which we can compare the Standard and Self-Absorption Models is the equilibrium case where charge-carriers are spread evenly across the sample thickness, in a 'flat' profile (shown in Figure S9). In this situation there will be no change in the shape of the charge-carrier distribution, so diffusion is irrelevant and the only difference between the two models is self-absorption.

Within the two models we can understand k_2 as describing different processes. In the Self-Absorption Model, k_2 is the photon generation rate in the material, and many of these emitted photons will be self absorbed. In the Standard Model, no self-absorption is accounted for and k_2 describes only the fraction of bimolecular decays which do not lead to re-absorption of photons. The two can be linked by the idea of an escape efficiency for PL, which is the probability that an emitted photon will be out-coupled from the material without being re-absorbed.

Using our current notation, Φ_2 in this case can also be described as the escape efficiency, and displays only a modest variation with film thickness, as shown in Figure S14. This slow variation arises as the high refractive index (2.5) of the perovskite and long PL absorption length mean that photon confinement, not film thickness, is the primary factor causing self-absorption. In this case Φ_2 is independent of the particular k_2 values used, and depends only on the film thickness. This relation between the intrinsic and apparent k_2 has been used in several other studies,[S10,S11] however, it is only applicable when there is a flat charge-carrier distribution.

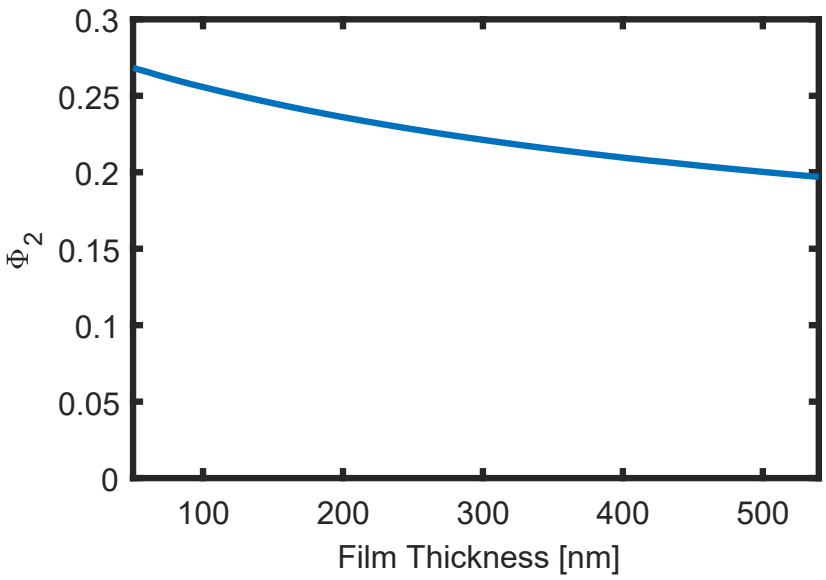

Figure S14: Modelled Φ_2 against film thickness for perovskite films on quartz, relating k_2 in the Standard and Self-Absorption Models, for the case where the n density profile is flat. The decay shown uses an intrinsic value of k_2 of 6.8 $\times 10^{-10}$ cm^{3}s^{-1} and a k_3 of 1 $\times 10^{-29}$ cm^{6}s^{-1}

7.3 Relating Standard and Self-Absorption Models in Pump-Probe Experiments

Building on the above results, we can now relate the Standard and Self-Absorption Models for the case where there is an initial Beer profile of charge-carriers, as is present in a pump-probe experiment. As the distribution of charge-carriers through the film in this case is uneven, self-absorption and diffusion will alter the charge-carrier distribution, causing the initial Beer profile to flatten out over time. However, the Standard Model does not allow the shape of the n profile to change, so the time-varying n profile of the Self-Absorption Model must be approximated by either a Beer or flat charge-carrier profile. Both of these profiles could arguably be used, as the Beer profile matches the initial charge-carrier distribution, while the flat profile matches the final charge-carrier distribution after self-absorption. The two models are compared by using the Self-Absorption Model to produce photo-conductivity decays, which are then fitted using the Standard Model and either a flat or Beer n profile. The suitability of each of these profiles in the Standard Model can be gauged by the degree to which Φ_2 depends on $k_2^{intrinsic}$ and k_3 of the Self-Absorption Model. If there is a consistent relation between the Self-Absorption and Standard Models, independent of the intrinsic recombination constants, then this can be used to link the two models. The less variation in Φ_2, the more robust the link between the two models and the more confidently we can relate the apparent and intrinsic values of k_2.

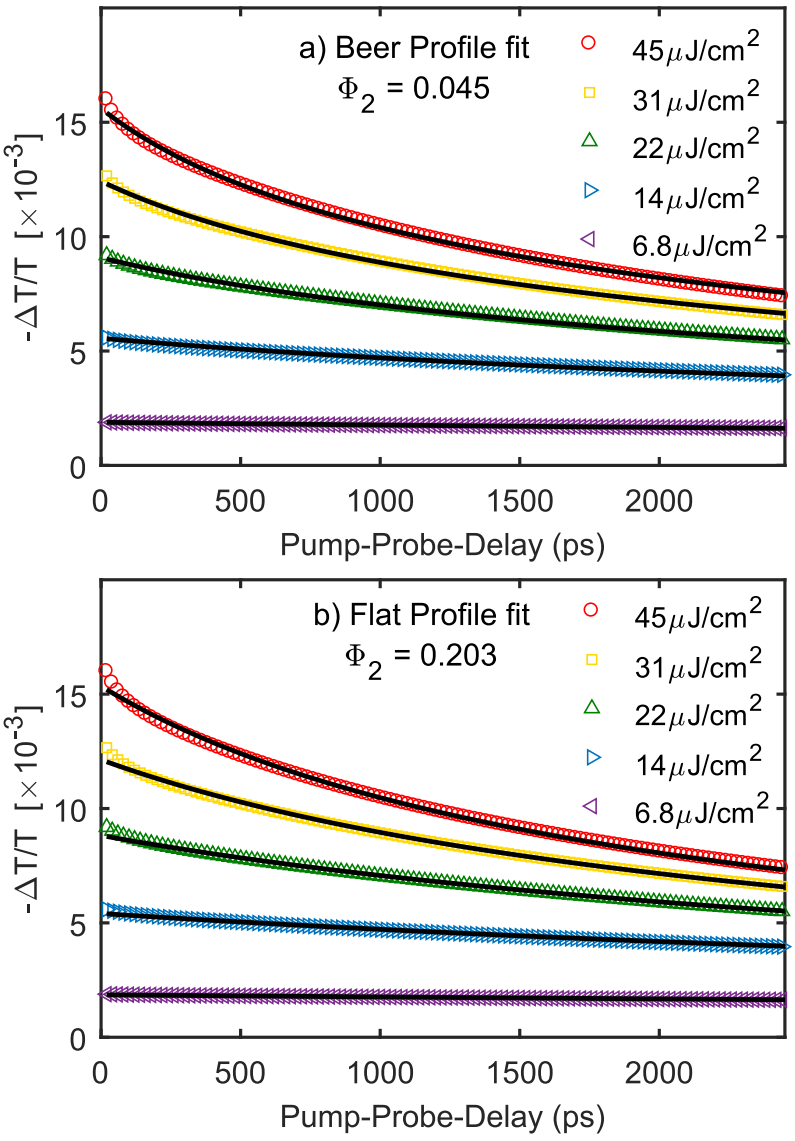

Figure S15: Modelled THz photo-conductivity transients in a 200 nm thick film, produced by the Self-Absorption Model and fitted in black lines by the Standard Model, using (a) a Beer and (b) a flat n profile. The Self-Absorption Model used the recombination constants $k_2 = 6.8\times10^{-10}$ cm^{3}s^{-1} and $k_3 = 1\times10^{-29}$ cm^{6}s^{-1}

The fits of the Standard Model, with each profile, to the photo-conductivity decays created by the Self-Absorption Model are shown in Figure S15, where it can be seen that the model fits the data well using either profile. However, the fit alone does not mean that the Standard Model is properly describing the underlying dynamics, as we know the charge-carrier dynamics follow a completely different pattern in the Self-Absorption Model. Therefore the wider relation between the two models across film thickness, presented in Figure S16, is important, so that Φ_2 can be established. It can be seen from Figure S16

that using the flat profile results in little variation in Φ_2 with thickness, whereas Φ_2 in the Beer profile shows a strong decrease as film thickness increases. This variation arises as the Beer profile does not assume the charge-carriers are spreading out across the film, whereas the flat profile assumes the charge carriers are fully spread out at each thickness. It is important to note that we have used the flat, not step profile here which would follow a similar decrease in Φ_2 to that for the Beer profile. By doing this we assume significant charge-carrier redistribution will occur, but the choice of profile will more generally depend on the strength of self-absorption in the system.

The exact form of the dependence of Φ_2 on thickness is actually unimportant, so long as it changes minimally as k_2 and k_3 in the Self-Absorption Model vary. Figure S15 shows how Φ_2 depends upon k_2 and k_3 and while for both profiles Φ_2 varies slowly, there are some differences. It can be seen from Figure S15a that Φ_2 changes more slowly for the flat profile than the Beer profile as k_2 is varied, at the same time, Figure S15b shows that with the Beer profile Φ_2 varies less as k_3 is changed. This behaviour arises because the Beer model more accurately describes the initial dynamics, when k_3 is most dominant and so can better isolate k_3 and k_2. Conversely, the flat model deals well with k_2 as the n profile at later times is flat and dominated by bimolecular recombination. The value of Φ_2 is further affected by α_{pump}, as shown in Figure 3b of the main manuscript, however, for a known value of α_{pump} the intrinsic k_2 can be estimated using the apparent value of k_2 and the relations described above.

While the relation between the Standard and Self-Absorption Models is here more complex than in the previous section, with careful consideration the two may be related. We note that this requires some knowledge of what self-absorption is likely present in the system and a careful choice of n profile. In our initial fits we chose to model the initial n as a Beer profile, to reflect the short absorption length, but in the case of a lower pump absorption coefficient, the flat profile may have proved more appropriate. Ultimately, any profile is an approximation of a changing charge-carrier distribution, and to extract the intrinsic recombination constants of a material the Self-Absorption Model is required.

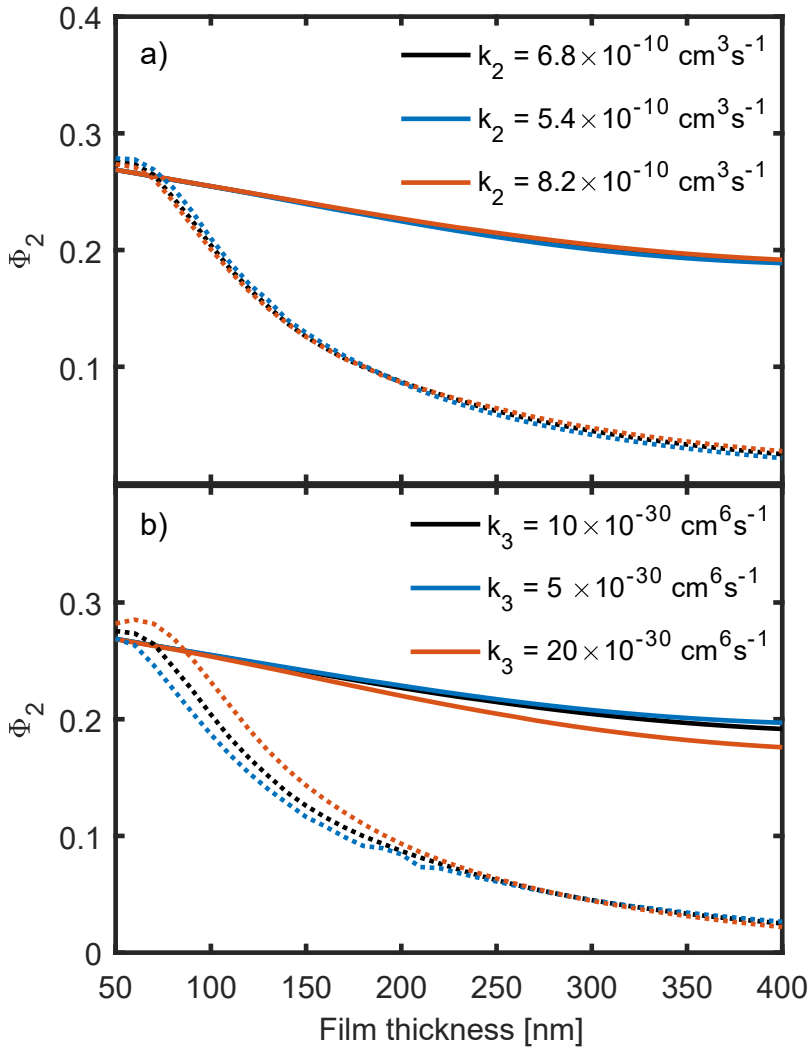

Figure S16: Modelled Φ_2 against film thickness, relating the Standard and Self-Absorption Models for a pump pulse with $\alpha = 4 \times 10^5$ cm^{-1}, incident upon a perovskite film on quartz. The solid lines show Φ_2 for a flat n profile, while dotted lines show the value for a Beer n profile (a) and (b) show how Φ_2 changes as k_2 and k_3, respectively, are varied in the Self-Absorption Model. The recombination constants set in the Self-Absorption Model are $k_2 = 6.8{\times}10^{-10}$ cm^{3}s^{-1} and $k_3 = 1{\times}10^{-29}$ cm^{6}s^{-1} unless otherwise labelled on the graph.

8 Additional Figures Displaying Charge-Carrier Recombination Dynamics

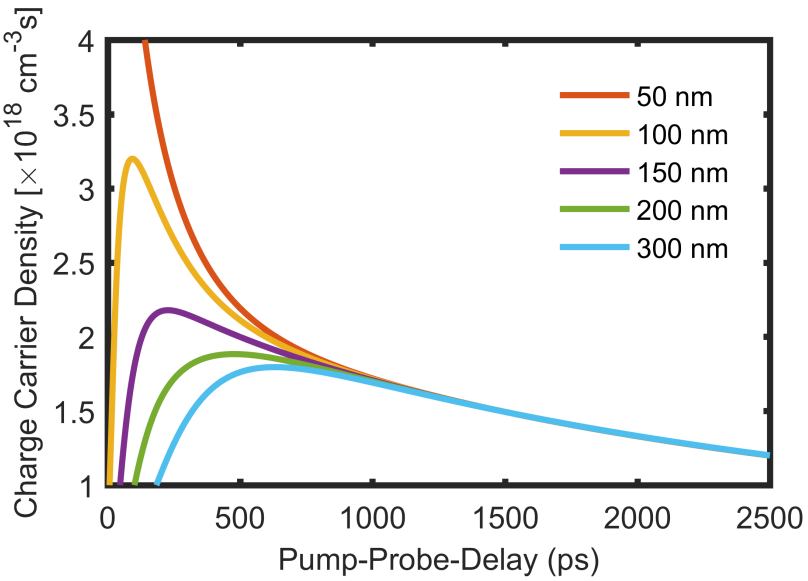

Figure S17: Modelled charge-carrier density at the labelled depths in a 300-nm thick film on quartz, for excitation at a wavelength of 400 nm with an incident pulse energy of 44 μJ/cm^2. These decays correspond to horizontal cuts across Figure 2a in the main script and are based on the Self-Absorption Model.

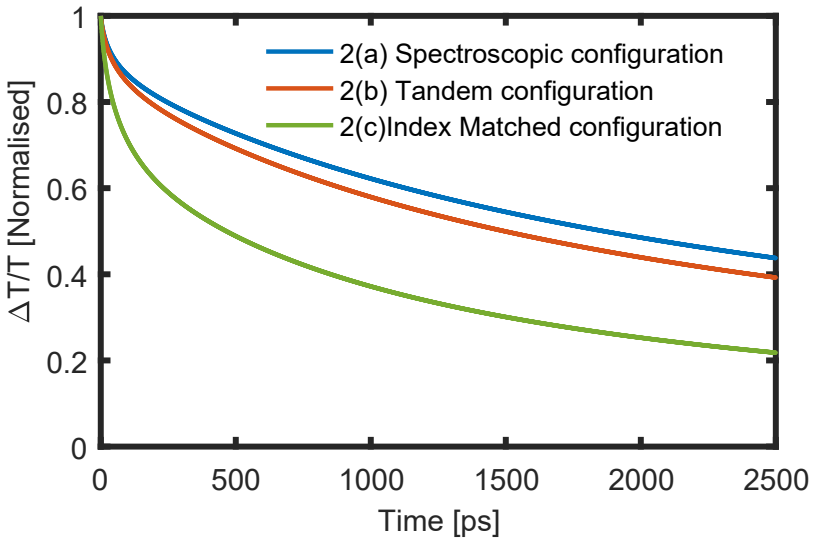

Figure S18: Photo-conductivity transients simulated using the Self-Absorption Model for each of the configurations shown in Figure 2 of the main manuscript, with excitation at a wavelength of 400 nm and an incident pulse energy of $44\mu J/cm^2$.

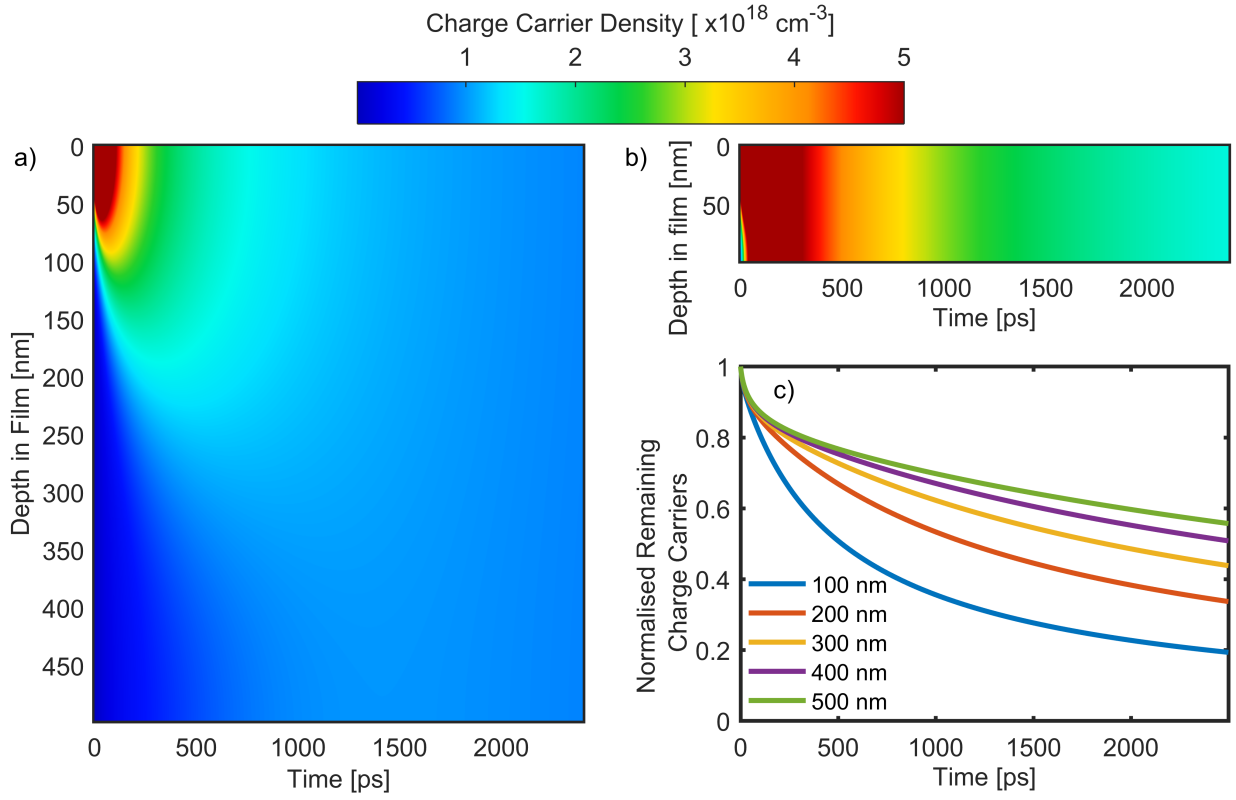

Figure S19: Modelled charge-carrier dynamics in a (a) 500-nm and (b) 100-nm perovskite film on quartz, for excitation at a wavelength of 400 nm with an incident pulse energy of 44 μJ/cm^2 using the Self-Absorption Model. (c) The normalised remaining charge-carrier populations for perovskite films with thickness range 100-500 nm, under the excitation conditions described above. The recombination constants used in each case are $k_2 = 6.8\times10^{-10}$ cm^{3}s^{-1} and $k_3 = 1\times10^{-29}$ cm^{6}s^{-1}.

9 Further Results from Self-Absorption Model

9.1 Modelling of $MAPbBr_3$

In this study we have limited our modelling to $MAPbI_3$, however, this is only one member of the hybrid metal halide perovskite family and so it is important to discuss how self-absorption will affect other compounds. To this end we now compare $MAPbI_3$ and the related $MAPbBr_3$, demonstrating how $k_2^{intrinsic}$ in the two materials may be much closer than previous reports have suggested, once self-absorption is accounted for.

In order to fully model the charge-carrier recombination within $MAPbBr_3$, a study of the PL spectrum and absorption profile would be needed, as the nature of self-absorption in a material will depend upon the exact overlap of the absorption and PL emission. However, we may gain some insight into the differences in the charge-carrier dynamics within the two materials by using certain approximations.

As iodide is replaced with bromide in $MAPb(Br_xI_{1-x})_3$ the bandgap increases from 1.55 to 2.3 eV[S9] (which is a useful means of tuning the bandgap for tandem applications). If we assume that the PL and absorption spectra maintain the same overlap when the halide is varied, the current modelling for self-absorption can be used for both materials. The only difference between the materials in a transient spectroscopy experiment will then be that due to the larger bandgap of $MAPbBr_3$, the absorption coefficient of the typical 400-nm pump excitation wavelength will be smaller, leading to an absorption length 4 times longer than in $MAPbI_3$.[S12] This is exactly the situation shown in Figure 3b of the main manuscript, where it was noted that both the charge-carrier lifetime and $k_2^{apparent}$ of a material in a pump-probe experiment will depend on the absorption length of the pump pulse. It was discussed that our modelling predicts $k_2^{apparent}$ to be a factor 4.2 larger in $MAPbI_3$ than $MAPbBr_3$, when the films are both 300 nm thick. Practically this means that, without accounting for self-absorption, we would determine the apparent k_2 to be 4.2 times larger in $MAPbI_3$, even if $k_2^{intrinsic}$ were the same as that of $MAPbBr_3$.

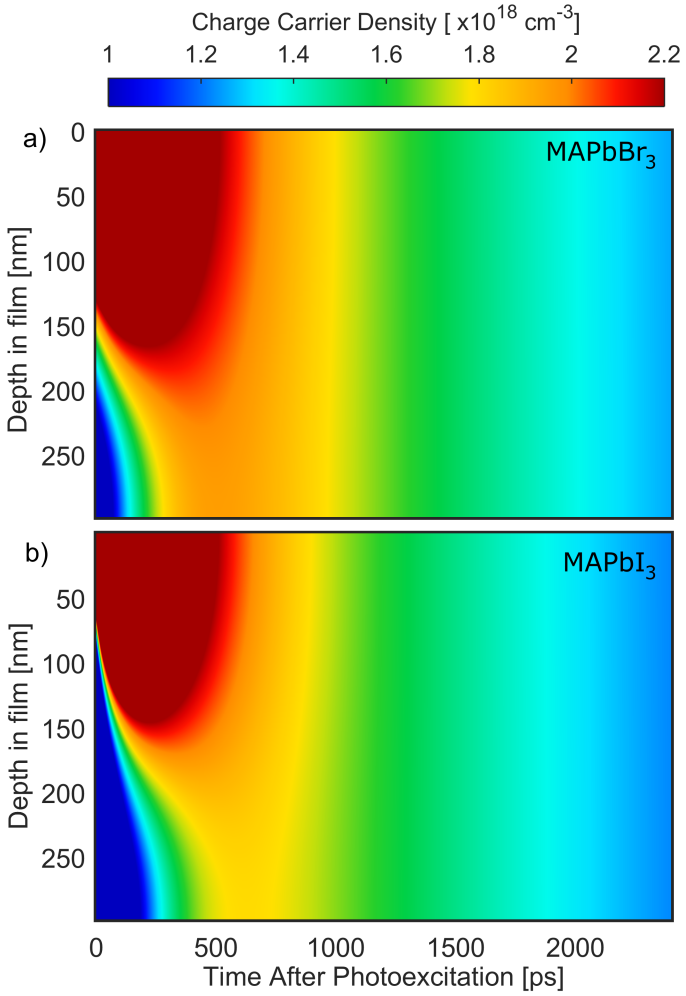

Figure S20: Modelled charge-carrier dynamics for 300 nm films of (a) $MAPbBr_3$ and (b) $MAPbI_3$ on quartz, for excitation at a wavelength of 400nm with an incident pulse energy of $45\mu J/cm^2$. The absorption coefficients used were $\alpha = 1 \times 10^5$ cm^{-1} for $MAPbBr_3$ and $\alpha = 4 \times 10^5$ cm^{-1} for $MAPbI_3$. Recombination constants used in each model were $k_2^{intrinsic}$ = $6.8{\times}10^{-10}$ cm^3s^{-1} and $k_3 = 1{\times}10^{-29}$ cm^6s^{-1}.

The reason for this difference comes from the previously discussed (see Section 7) inability of the Standard Model to deal with the redistribution of charge-carriers within the film. Figure S20 shows the modelled charge-carrier dynamics in $MAPbI_3$ together with those for $MAPbBr_3$, under the assumption that both have the same bimolecular recombination constants and self-absorption, but different initial absorption lengths at the excitation wavelength. In both cases, the initial Beer profile swiftly flattens out as self-absorption and diffusion cause charge-carrier redistribution, and from that point onwards the two decays are identical. This is reflected in the modelled photo-current transients of the two modelled materials, shown in Figure S21, which show the simulated charge-carrier population decay for each material. Initially $MAPBI_3$ shows faster charge-carrier recombination arising from the

higher initial charge-carrier densities created by the short pump absorption length, however, after 1 ns the charge-carrier distribution in both cases is flat and so the decays are therefore similar. In fitting these decays with the Standard Model, a different n will be assumed in each case, because of the different pump absorption lengths, thereby creating the difference in $k_2^{apparent}$.

Applying this idea to previous studies, in one case the reported value of k_2 (i.e. $k_2^{apparent}$) was found to be 3.3 times larger in $MAPbBr_3$ than in $MAPbI_3$,[S13] where our model predicts a factor 5 between the $k_2^{apparent}$ of the two materials, at the film thickness used in the study. This means that, although we have not accounted for any differences in self-absorption, the $k_2^{intrinsic}$ of the two materials are likely much closer than predicted. This may further suggest that the reported increase in the recombination rate, as the halide composition varies from $MAPbI_3$ to $MAPbBr_3$, may be in part explained by the changing absorption coefficient at the pump wavelength, rather than a change in $k_2^{intrinsic}$. However, to confirm this, the self-absorption in $MAPbBr_3$ will have to be accurately accounted for.

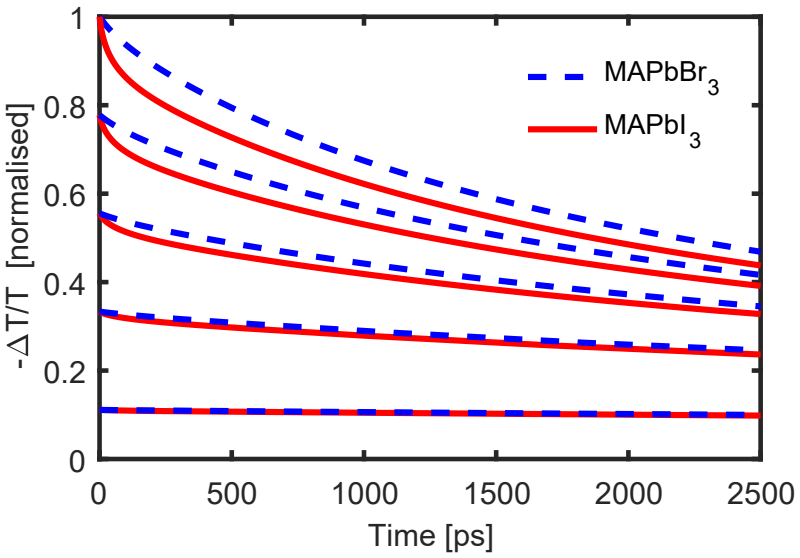

Figure S21: Simulated photo-conductivity transients for 300-nm thick films of (a) $MAPbBr_3$ and (b) $MAPbI_3$ on quartz, based on the Self-Absorption Model. The Pump excitation fluences assumed in the model are 45, 25 and 15 $\mu J/cm^2$. Both sets of decays share the same underlying recombination constants with $k_2^{intrinsic} = 6.8\times10^{-10}\,cm^3s^{-1}$ and $k_3 = 1\times10^{-29}\,cm^6s^{-1}$.

9.2 Relative Contributions of Diffusion and Self-Absorption

Our Self-Absorption Model incorporates both charge-carrier diffusion and self-absorption, however, by selectively removing each of these terms from the model, the separate impact of the two processes can be evaluated. Figure S22 compares how the charge-carrier dynamics in a film, modelled with the same recombination constants, change as diffusion and self-absorption are excluded or accounted for. Figure S23 shows the corresponding photoconductivity decays, which are directly proportional to the total charge-carrier population in each case.

In Figure S22a, neither diffusion or self-absorption are accounted for and the Self-Absorption Model has been reduced back to the Standard Model. As the only remaining processes are charge-carrier recombination, the charge-carriers do not spread out and, as displayed in Figure S23, the total charge-carrier population drops away swiftly.

When self-absorption is included, there is now a much slower decay in the overall charge-carrier population, as only a fraction of bimolecular recombination events now result in the escape of a photon. There is now also a steady redistribution of the charge-carriers across the film, due to the effect of re-absorption.

In the case where only diffusion is accounted for, there is a fast initial spreading out of the charge-carriers, giving the appearance in Figure S22(c) that the decay is faster here than when there is no diffusion. In fact, Figure S23 shows that the total charge-carrier population actually decays more slowly, as higher-order recombination is made less efficient by the lowering of n from diffusion. The decay only appears faster in Figure S22(c) as regions of high n are being spread out by diffusion.

Finally, as both processes are included, the charge-carrier dynamics can be seen to be governed by a mix of diffusion and self-absorption. Combining both the initial charge-carrier diffusion and the larger-scale redistribution from self-absorption, it can be seen from Figure S22(d) that the charge-carriers now become evenly spread across the film after only 1 ns.

Analysing the total charge-carrier population decay, in Figure S23 it can be clearly seen that each process reduces charge-carrier losses in a different portion of the decay. Most obviously there is a reduction in bimolecular recombination losses from self-absorption which remains important throughout the decay and will do, so long as bimolecular recombination remains significant. Additionally, within the first 100 ps, diffusion slows the rate of charge-carrier recombination, as it will make both bimolecular and Auger recombination less efficient by spreading out charge carriers and lowering n. After this time window the n profile is much flatter and diffusion becomes less important, particularly in the case where self-absorption is also redistributing charge-carriers. The combination of these two processes thereby leads to a much slower decay of the total charge-carrier population than when they are omitted.

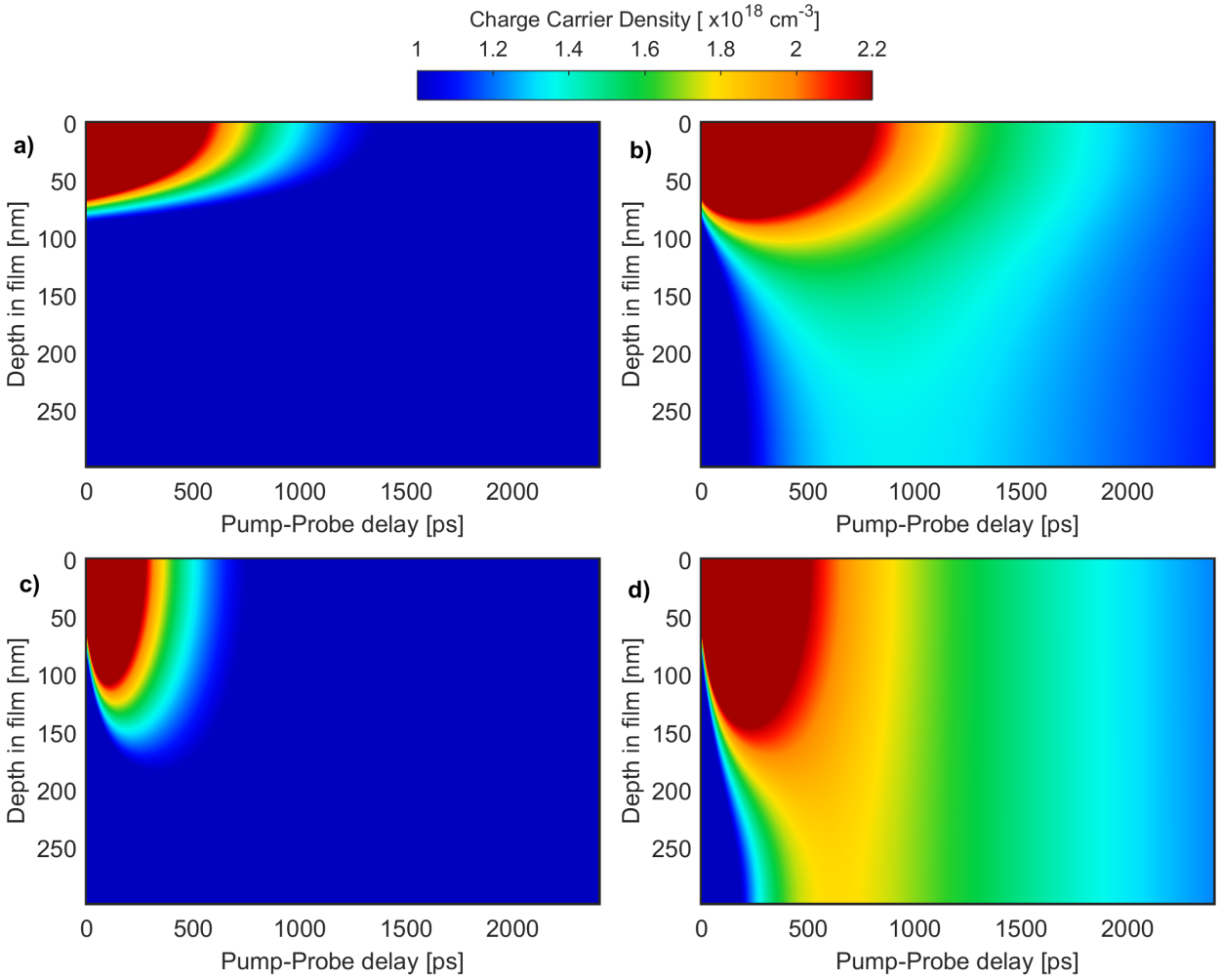

Figure S22: Modelled charge-carrier dynamics for 300 nm films of $MAPbI_3$ on quartz, where (a) neither diffusion nor self-absorption, (b) only self-absorption, (c) only diffusion and (d) both diffusion and self-absorption are/is accounted for. In each case the recombination constants used were $k_2 = 6.8\times10^{-10}\,\mathrm{cm^3s^{-1}}$ and $k_3 = 1\times10^{-29}\,\mathrm{cm^6s^{-1}}$ and excitation was assumed to be at 400 nm with an incident pulse energy of 45 $\mu\mathrm{J/cm^2}$.

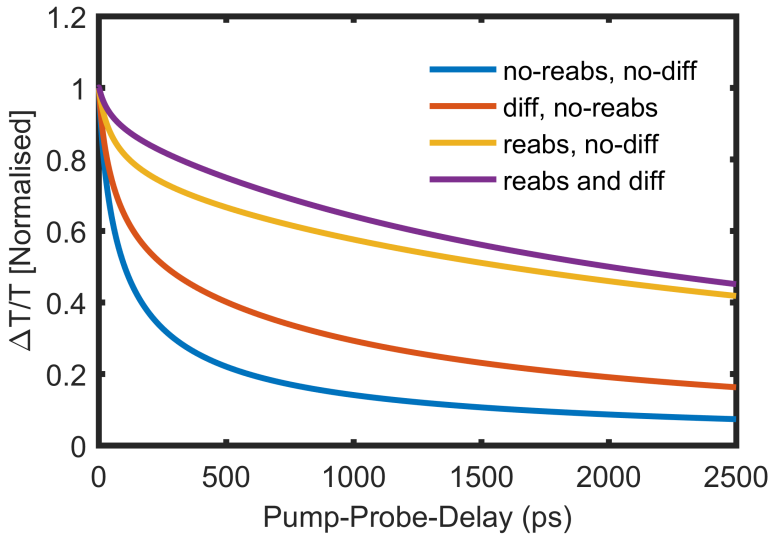

Figure S23: Modelled photo-conductivity transients for a 300 nm film of $MAPbI_3$ on quartz, where charge-carrier diffusion and self-absorption are either included or ignored, as in Figure S22.

References

(S1) Patel, J. B.; Wong-Leung, J.; Van Reenen, S.; Sakai, N.; Wang, J. T. W.; Parrott, E. S.; Liu, M.; Snaith, H. J.; Herz, L. M.; Johnston, M. B. Influence of Interface Morphology on Hysteresis in Vapor-Deposited Perovskite Solar Cells. *Adv. Electron. Mater.* **2016**, *3*, 1600470.

(S2) Schlipf, J.; Müller-Buschbaum, P. Structure of Organometal Halide Perovskite Films as Determined with Grazing-Incidence X-Ray Scattering Methods. *Adv. Energy Mater.* **2017**, 16146840.

(S3) Oesinghaus, L.; Schlipf, J.; Giesbrecht, N.; Song, L.; Hu, Y.; Bein, T.; Docampo, P.; Müller-Buschbaum, P. Toward Tailored Film Morphologies: The Origin of Crystal Orientation in Hybrid Perovskite Thin Films. *Adv. Energy Mater.* **2016**, *3*, 21967350.

(S4) Harbecke, B. Coherent and Incoherent Reflection and Transmission of Multilayer Structures. *Appl. Phys. B* **1986**, *39*, 165–170.

(S5) Wehrenfennig, C.; Liu, M.; Snaith, H. J.; Johnston, M. B.; Herz, L. M. Charge-carrier dynamics in vapour-deposited films of the organolead halide perovskite $CH_3NH_3PbI_{3x}Cl_x$. *Energy & Environmental Science* **2014**, *7*, 2269.

(S6) Milot, R. L.; Eperon, G. E.; Snaith, H. J.; Johnston, M. B.; Herz, L. M. Temperature-Dependent Charge-Carrier Dynamics in $CH_3NH_3PbI_3$ Perovskite Thin Films. *Adv. Funct. Mater.* **2015**, *25*, 6218–6227.

(S7) Trinh, M. T.; Wu, X.; Niesner, D.; Zhu, X. Many-Body Interactions in Photo-Excited Lead Iodide Perovskite. *J. Mater. Chem. A* **2015**, *3*, 9285–9290.

(S8) Wehrenfennig, C.; Eperon, G. E.; Johnston, M. B.; Snaith, H. J.; Herz, L. M. High charge carrier mobilities and lifetimes in organolead trihalide perovskites. *Adv. Mater.* **2014**, *26*, 1584–1589.

(S9) Rehman, W.; Milot, R. L.; Eperon, G. E.; Wehrenfennig, C.; Boland, J. L.; Snaith, H. J.; Johnston, M. B.; Herz, L. M. Charge-Carrier Dynamics and Mobilities in Formamidinium Lead Mixed-Halide Perovskites. *Adv. Mater.* **2015**, *27*, 7938–7944.

(S10) Pazos-Outon, L. M.; Szumilo, M.; Lamboll, R.; Richter, J. M.; Crespo-Quesada, M.; Abdi-Jalebi, M.; Beeson, H. J.; Vrucinic, M.; Alsari, M.; Snaith, H. J.; Ehrler, B.; Friend, R. H.; Deschler, F. Photon recycling in lead iodide perovskite solar cells. *Science* **2016**, *351*, 1430–1433.

(S11) Ha, S.-T.; Shen, C.; Zhang, J.; Xiong, Q. Laser cooling of organic-inorganic lead halide perovskites. *Nat. Photon.* **2015**, *10*, 115–121.

(S12) Leguy, A.; Azarhoosh, P.; Alonso, M. I.; Campoy-Quiles, M.; Weber, O. J.; Yao, J.; Bryant, D.; Weller, M. T.; Nelson, J.; Walsh, A.; van Schilfgaarde, M.; Barnes, P. R. F. Experimental and theoretical optical properties of methylammonium lead halide perovskites. *Nanoscale* **2015**, *8*, 6317–6327.

(S13) Yang, Y.; Yang, M.; Li, Z.; Crisp, R.; Zhu, K.; Beard, M. C. Comparison of Recombination Dynamics in $CH_3NH_3PbBr_3$ and $CH_3NH_3PbI_3$ Perovskite Films: Influence of Exciton Binding Energy. *J. Phys. Chem. Lett* **2015**, *6*, 4688–4692.